PAPER • OPEN ACCESS

The potential of imogolite nanotubes as (co-)photocatalysts: a linear-scaling density functional theory study

To cite this article: E Poli *et al* 2016 *J. Phys.: Condens. Matter* **28** 074003

View the article online for updates and enhancements.

The potential of imogolite nanotubes as (co-)photocatalysts: a linear-scaling density functional theory study

E Poli[1],[6], **J D Elliott**[1],[6] **L E Ratcliff**[2], **L Andrinopoulos**[2], **J Dziedzic**[3],[4],
N D M Hine[5], **A A Mostofi**[2], **C-K Skylaris**[3], **P D Haynes**[2] and **G Teobaldi**[1]

[1] Stephenson Institute for Renewable Energy and Department of Chemistry, University of Liverpool, Liverpool L69 3BX, UK
[2] The Thomas Young Centre for Theory and Simulation of Materials, Imperial College London, London SW7 2AZ, UK
[3] School of Chemistry, University of Southampton, Southampton SO17 1BJ, UK
[4] Faculty of Applied Physics and Mathematics, Gdansk University of Technology, Gdansk, Poland
[5] Department of Physics, University of Warwick, Coventry CV4 7AL, UK

E-mail: g.teobaldi@liv.ac.uk

Abstract

We report a linear-scaling density functional theory (DFT) study of the structure, wall-polarization absolute band-alignment and optical absorption of several, recently synthesized, open-ended imogolite (Imo) nanotubes (NTs), namely single-walled (SW) aluminosilicate (AlSi), SW aluminogermanate (AlGe), SW methylated aluminosilicate (AlSi-Me), and double-walled (DW) AlGe NTs. Simulations with three different semi-local and dispersion-corrected DFT-functionals reveal that the NT wall-polarization can be increased by nearly a factor of four going from SW-AlSi-Me to DW-AlGe. Absolute vacuum alignment of the NT electronic bands and comparison with those of rutile and anatase TiO_2 suggest that the NTs may exhibit marked propensity to both photo-reduction and hole-scavenging. Characterization of the NTs' band-separation and optical properties reveal the occurrence of (near-)UV inside–outside charge-transfer excitations, which may be effective for electron–hole separation and enhanced photocatalytic activity. Finally, the effects of the NTs' wall-polarization on the absolute alignment of electron and hole acceptor states of interacting water (H_2O) molecules are quantified and discussed.

Keywords: photocatalysis, inorganic nanotubes, imogolite nanotubes, linear-scaling density functional theory

S Online supplementary data available from stacks.iop.org/JPhysCM/28/074003/mmedia

(Some figures may appear in colour only in the online journal)

1. Introduction

As the costs of energy production increase, due to both limitation of resources and the impact of an oil-fuelled economy on the climate, the interest in materials and technologies capable of converting sunlight into commercially viable forms of energy such as electrical current or chemical fuels has been steadily growing [1–3]. Crucial to this energy conversion is the availability of photocatalysts (PCs). PCs are substances capable of generating, upon light absorption, highly reactive excited electron–hole (e*-h) pairs that may eventually transfer excited state energy or, following their separation, enter an electric circuit or be transferred to reactants. These processes

can then be used to produce electrical power, chemical fuels and feedstocks, to decompose pollutants, and even for virus or bacteria disinfection [1–12].

In general [1–13], the efficiency and viability of a given PC is jointly determined by the following elements: (i) the PC needs to be able to absorb light via electronic excitation. For sunlight and artificial visible light to be used, the energy gap between occupied and empty electronic states of the PC need to match the visible light spectrum (1.6–3.1 eV) and ideally the sun radiance peak (1.6–2.1 eV) [14]. (ii) The nature of the electronic excitation or its decay needs to lead to effective separation of the excited electron (e*) and hole (h), preventing their recombination. (iii) The separated e* and h must diffuse efficiently and independently to the surface of the PC (or the current collectors for photovoltaics application [14]). (iv) For photocatalytic applications, the photogenerated excited e* and h need to be transferred to reactants with high efficiency. Efficient transfer of e* (photoreduction) or h (photo-oxidation) rests on suitable alignment between the PC and reactant electronic energy levels as well as electron-transfer kinetics faster than any competitive e*-h recombination process. (v) The transfer of photogenerated e* or h needs to lead to the desired product(s). Furthermore, and ideally, (vi) the ratio of absorbed photons to e* (h) transferred and generated product (quantum yield) should be as high as possible [1–13], and (vii) the selectivity of a given PC towards a specific reactant or product in a multi-component medium should be controllable and tuneable [15].

Over a century of research in the field [1–13, 16–19] has firmly established that, besides being a formidable challenge, simultaneous fulfilment of conditions (i)–(vii) intimately depends on the atomic composition, structure and dynamics of the PC, reactants and their interfaces in a given medium. In spite of this, the current understanding of the atomistic requirements to maximise the efficiency of a given PC for a given reaction is far from exhaustive. As a result, great efforts are now directed towards atom- and time-resolved characterization of PCs and their interfaces with reactants in different media. Improved atomistic understanding of PCs would greatly expedite the development of novel photocatalytic solutions [1–19].

Given the experimental challenges (and costs) in time- and atom-resolved characterization of photocatalytic interfaces, and the increasing accuracy of first-principles simulation methods, modelling of PCs and their interfaces has become an important component in fundamental research in photocatalysis [20–27]. This is because modelling can relatively inexpensively access the atomic and electronic factors underpinning the physical and chemical functioning of PCs. Furthermore, as presented and discussed here, modelling can be also used to single out elements hardly accessible to experimental analysis, which could be used to develop novel photocatalytic strategies.

Since an extended account of the remarkably broad literature on photocatalysis is beyond the scope of this paper, we refer the reader to recent review articles [1–13, 17–19]. To better discuss the results presented below, here we limit ourselves to briefly summarising three emerging strands of research in photocatalysis, namely, the development of one-dimensional (1D) nanostructured or ferroelectric PCs for enhanced e*-h

separation and diffusion to PC surfaces, and the exploitation of nano-confinement effects to control selectivity in porous PCs.

The increased aspect ratio (the ratio of length to diameter or surface to volume) of 1D nanostructures has been recently shown to be linked to an increased photocatalytic activity as a result of the highly anisotropic diffusion of separated e*-h pairs in CdS, ZnO and GaN nanorods [28–30]. The possibilities offered by nano-engineering the micro-facets exposed by 1D TiO_2 and Zn_2GeO_4 substrates have been recently explored, revealing clear benefits with respect to bulk or thin-film phases [31–33]. Coating or asymmetric functionalization of 1D nanostructured substrates has also started to be studied, with findings offering appealing prospects for development of enhanced photocatalytic strategies [19, 34–43].

The pivotal role of an effective e*-h separation for any viable photocatalytic strategy has led to a growing interest in the development of photo-active ferroelectric substrates. These possess intrinsic permanent polarizations, which are capable of biasing the e*-h relaxation, leading to efficient separation and diffusion to the PC surfaces. Reports on the beneficial role that permanent polarizations can play for efficient e*-h separation have started to appear in the literature [44–50], prompting growing interest in this field. To the best of our knowledge, the use of 1D ferroelectrics for photocatalysis is yet to be explored, although several studies of 1D ferroelectric nanotubes (NTs) and nanorods are present in the literature [51–66].

Together with efficiency, cost and scalability, selectivity of the PC is another critical element for controlled, industrially viable synthesis and conversion of fine-chemicals and feedstock. Stimulated by pioneering work on highly selective methane activation by microporous beta-zeolite via deep-UV photocatalysis [15], the concept of nanoconfinement-assisted photocatalysis has started to receive attention from both experimental and theoretical communities [67–72].

The fast-paced, yet to date disconnected, progress in development of photocatalytic strategies based on 1D nanostructures [19, 28–34], ferroelectric substrates [44–50] and porous PCs [67–72] has led us to question whether these three concepts could be integrated in one solution, ideally based on cheap and abundant materials. In addition, we speculate on whether local polarization of overall dipole-free nanostructures, rather than macroscopic polarizations present in ferroelectrics, could be as effective in promoting e*-h separation and enhance photocatalytic activity. To this end, atomically resolved insight into the relationships that exist between the local electrostatics of a porous photocatalyst, its local polarizations, the vacuum-alignment and real-space distribution of electron bands, as well as the ensuing perturbations to the reactant electronic states would be a highly beneficial complement to research in the field.

Towards preliminary exploration of these concepts, here we investigate the electronic and optical properties as well as the effects on interacting H_2O molecules, of a class of 1D nanomaterial, imogolite (Imo) NTs, which has been receiving growing interest from the experimental and theoretical community [73–114].

Imogolite aluminosilicate (AlSi) and aluminogermanate (AlGe) NTs are structurally analogous to the naturally occurring hydrous-aluminosilicate imogolite [81–83]. Its walls
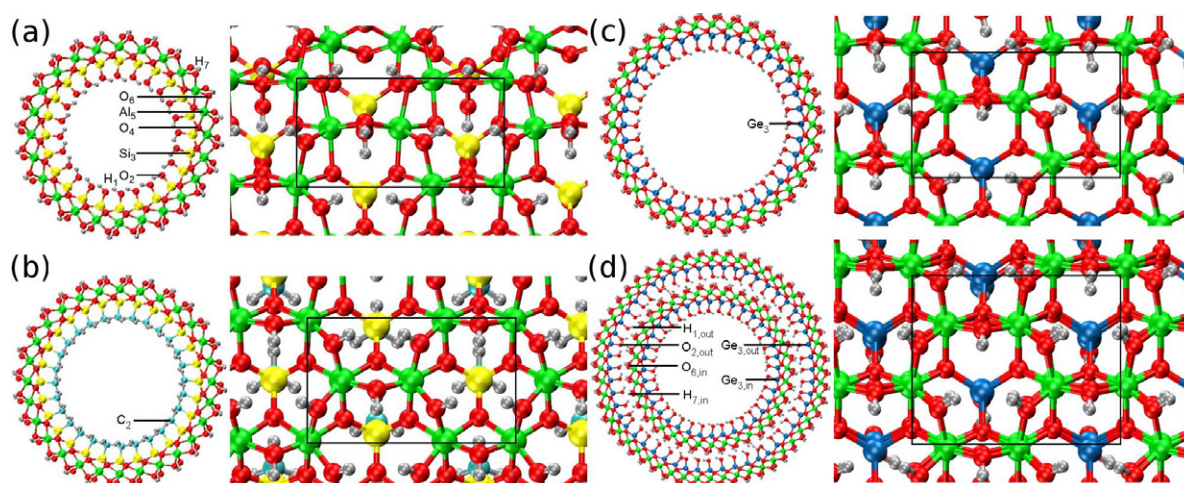
Figure 1. Top and side view of the optimized (a) SW-AlSi$_{24}$, (b) SW-AlSi$_{28}$-Me, (c) SW-AlGe$_{36}$ and (d) DW-AlGe$_{36,54}$ Imo NTs. The zigzag periodic unit along the nanotube axis is marked by the black rectangle. The adopted radial labelling is displayed in panel (a), with O$_2$ being substituted by C$_2$ in (b). Si$_3$ is substituted by Ge$_3$ in (c), and by Ge$_{3,in}$ and Ge$_{3,out}$ in (d). Al: green, Si: yellow, Ge: blue, O: red, H: silver, C: cyan.

consist of a single layer of octahedrally coordinated aluminum hydroxide (gibbsite) with pendant tetrahedral silanol (Si–OH) groups facing the tube cavity (figure 1). From a compositional point of view, the only difference between AlSi and AlGe NTs is the substitution of silanol groups with germanol (Ge–OH) groups. The resulting chemical formulae of the unit cells are (Al$_2$SiO$_7$H$_4$)$_N$ and (Al$_2$GeO$_7$H$_4$)$_N$ for Al–Si and Al–Ge tubes, respectively, with N being the number of radially non-equivalent aluminum atoms along the NT circumference, an even number for symmetry reasons [84].

Over the last few years, the understanding and control of the growth of these materials has progressed noticeably, with the definition of solution-based synthetic routes to single-walled (SW) AlSi and AlGe NTs of controllable radius and length [73–85]. In addition, the creation of double-walled (DW) AlGe NTs has also been achieved [86–89]. Important advances have been made in the post-synthetic, selective functionalization of the outer or inner surface of AlSi NTs [90–92], and in the direct creation of methylated (AlSi-Me) [93, 94] or aminated (AlSi-Am) [95] AlSi NT derivatives, with methyl (–CH$_3$, figure 1) or amine (–NH$_2$) functions in the NT cavity as well as in the synthesis of hybrid methylated Al(Si/Ge)-Me NTs with tuneable Si/Ge ratio [96]. Further selective amination of the outer surface of AlSi-Me NTs by post-synthesis grafting, yielding hybrid Am-AlSi-Me derivatives, has also been reported [91, 92]. Exploration of the surface properties of these hybrid materials has revealed superior performances for chemical separation [91–96], and results on their beneficial role as support for (photo)catalysts [97, 98] as well as in hybrid nanocomposites [99] have started to appear in the literature. Recent progress in the controlled synthesis of Fe-doped AlSi and AlGe NTs [100–102] holds great promise for reducing Imo NTs' band gap (BG) to match sunlight and for the introduction of enhanced (photo)catalytic properties in Imo NTs.

Besides the highly controllable and reproducible synthesis of these photoactive, water-soluble systems and their ease of functionalization [73–99], our interest is motivated by the presence of a permanent polarization of the tube-wall and a real-space separation of the valence (VB) and conduction band (CB) edges of pristine Imo NTs [106, 107, 112], which suggest potentially favourable e*-h separation, thence significance for photocatalysis. Furthermore, the superior chemical-separation properties of hybrid hydrophobic/hydrophilic Imo NTs and their ease of functionalization [91–96] could be extremely beneficial for efficient separation of photo-oxidised and photo-reduced reactants and products, potentially allowing integration of 'Z-schemes' [115, 116] across the NT-wall.

Although density functional theory (DFT) modelling and derived tight-binding approximations (TB-DFT) have assisted research in the growth mechanism of AlSi NTs [79, 80], in the properties of periodic defect-free (SW and DW) AlSi and AlGe NTs models [103–109], and in possible phosphorous- and arsenic-based functionalization [110], the recent experimental progress in the field of Imo-NTs has yet to be completely matched by the materials modelling community. With the exception of a very limited number of DFT studies of point-defects and Fe-doping in AlSi and AlGe NTs [105, 106, 111], the structural and electronic characterization of defects, dopant, functionalization and termination effects in Imo-NTs and their role in tuning the NT electronic and spectroscopic properties as well as its chemical reactivity is to date unexplored. In addition, AlSi NTs walls are known from experiments to develop an intrinsic polarization [112], with accumulation of negative (positive) charges on the interior (exterior) of the NT-cavity. DFT simulations have shown this polarization to be linked with a separation in real space of the NT VB and CB edges [106, 107], and to be independent of the substitution of Si–OH by Ge–OH in the tube interior [106]. The extent to which these appealing AlSi and AlGe NT properties are affected by functionalization of the tube walls [90–96], encapsulation of NTs of different radii in double-walled AlGe NTs [87–89], cation-vacancy induced defects [113] or by the ionic strength of the solvent is currently unknown, which motivates our interest in this class of materials.

DFT-based research in the field of Imo-NTs has so far been hindered by the severe accuracy-viability compromises, which need to be faced when modelling this class of systems on academically available hardware, even on Tier-1 high performance computing systems. With a periodic unit cell containing over 300 atoms for the smallest member of the Imo-NT family, the AlSi ($N = 24$) NT with 336 atoms [84], the computational effort required for standard plane-wave or atomic basis-set simulation of these systems is, at the very least, challenging. As a result, with to date a single exception [114], DFT investigations of Imo-NTs have been limited to periodically repeated models of no more than one periodic ring [103–110] or fractions of the Imo-NT circumference [79, 80]. Although reduction of the computational cost of the simulations can be obtained by using a minimal (fixed) atomic-basis set [103, 105, 107, 111], exploiting symmetry [108], or relying on the transferability of TB-DFT parameterizations for analogous systems [104, 109], best practice for accurate simulation of these systems in the presence of defects, dopants, termination effects, electronic excitations and solvation by media of non-negligible ionic-strength is far from being established.

The well-known limitations of standard local and semi-local exchange-correlation functionals in accurate simulation of BGs, electronic localization and polaronic distortions in metal-oxide materials [117–119] further increase the range of challenges and accuracy compromises to be faced for realistic modelling of Imo-NTs at standard DFT-level. Such compromises can however be ameliorated by realization of the remarkable progress made in linear-scaling implementations of DFT (LS-DFT), which have made it possible to simulate systems up to several thousand atoms at DFT-level on academically available hardware [120], and have been recently benchmarked on Imo NTs [114]. Following this initial computational benchmark, here we present an exploration using LS-DFT of the relationships between the composition of Imo NTs and their electronic and optical properties as well as their potential as model systems for the development of novel photocatalytic strategies based on inorganic nanotubes.

The manuscript is organized as follows: after a brief introduction to the computational methods adopted (section 2), in section 3 we present and discuss results on the structural and electronic characterization, absolute band alignment and wall-polarization for pristine SW AlSi NTs as well as SW AlSi-Me, SW AlSiGe and DW AlGe NTs for different DFT functionals and treatment of dispersion interactions. We then analyse the optical absorption properties of the systems considered and discuss them against available experimental data. Finally, we investigate and quantify the effects of the (different) NT wall-polarization on the absolute alignment of H_2O electron acceptor and donor states for model NT/H_2O interfaces.

2. Methods

2.1. Linear-scaling DFT in ONETEP

In this section, we briefly present the theoretical framework behind linear-scaling DFT (LS-DFT) and its implementation

in the ONETEP program [121–124]. The interested reader is referred to [120] for a recent review of LS-DFT methods.

Linear-scaling methods make use of the 'nearsighted-ness' [125, 126] inherent in quantum many-body systems by exploiting the localization of Wannier functions [127–130] or the single-particle density matrix, $\rho(\mathbf{r}, \mathbf{r}')$ [131, 132]. ONETEP is based on the latter approach and on a formulation of DFT theory with norm-conserving pseudopotentials [133]. Within ONETEP $\rho(\mathbf{r}, \mathbf{r}')$, is expressed in a separable form [134, 135] via atom-centred functions (non-orthogonal generalized Wannier functions, NWGFs [84]), $\phi_\alpha(\mathbf{r})$, as:

$$\rho(\mathbf{r},\mathbf{r'}) = \sum_{\alpha\beta} \phi_\alpha(\mathbf{r})K^{\alpha\beta}\phi_\beta^*(\mathbf{r'}) \tag{1}$$

where $K^{\alpha\beta}$ are the matrix elements of the density kernel, which are nonzero only if $|\mathbf{r}_\alpha - \mathbf{r}_\beta| < r_c$, where $\mathbf{r}_\alpha$ and $\mathbf{r}_\beta$ indicate the coordinates of the centres of ϕ_α and ϕ_β, and r_c is a real-space cut-off threshold. The (optional) truncation of the density kernel ($K^{\alpha\beta}$), leading to a sparse density matrix $[\rho(\mathbf{r}, \mathbf{r}')]$ is justified by the known exponential decay of $\rho(\mathbf{r}, \mathbf{r}')$ with respect to $|\mathbf{r} - \mathbf{r}'|$ for systems with an electronic BG [130–132], which makes any insulating or semiconducting systems (including the Imo-NTs considered here) amenable to LS-DFT simulation.

The NGWFs are centred on the nuclear coordinates and strictly localized within a sphere of radius R_α. Being non-orthogonal, the NGWFs are characterized by a non-diagonal overlap matrix, $S_{\alpha\beta}$:

$$S_{\alpha\beta} = \int d\mathbf{r}\phi_\alpha^*(\mathbf{r})\phi_\beta(\mathbf{r}). \tag{2}$$

The NGWFs are in turn expanded as a linear combination, of coefficients $C_{m\alpha}$, of localized yet orthogonal periodic cardinal sine (*psinc*) functions [136], $D_m(\mathbf{r})$, as:

$$\phi_\alpha(\mathbf{r}) = \sum_m C_{m\alpha}D_m(\mathbf{r} - \mathbf{r}_m) \tag{3}$$

with m indexing the real-space Cartesian grid inside the spherical localisation region of ϕ_α. The *psinc* functions are formed from a discrete sum of plane-waves, which makes the set of $D_m(\mathbf{r})$ independent of the nuclear coordinates and systematically improvable upon increase of the kinetic energy cutoff [133]. In the ONETEP approach, the total DFT energy is minimized self-consistently with respect to $K^{\alpha\beta}$ and $C_{m\alpha}$ in two nested loops [121–124]. As a result, the NGWFs are optimized *in situ* by iteratively improving the set of coefficients $C_{m\alpha}$ that minimize the total energy under the constraints of idempotency of the density matrix ($\rho^2 = \rho$) and conservation of the number of electrons in the simulated system. The approach has been shown to lead to convergence of results to a near complete basis set quality even for minimal number of NGWFs employed in the simulations [137].

An alternative approach to self-consistent energy minimization is to instead employ a single loop that optimizes the elements of $K^{\alpha\beta}$ only, maintaining the NGWFs fixed. Recent additions to ONETEP allow generation of suitable multiple-zeta basis sets out of pseudoatomic orbitals (PAOs), which can also be used with high accuracy given a large enough basis

and the explicit calculation of the Pulay forces arising from incomplete optimization of the basis set [138].

As discussed in [121–124], the convergence of the ONETEP approach can depend on interlinked computational factors such as the kinetic energy cutoff, the number of NGWFs (ϕ_α) per atom and their localization radius. The reader if referred to [114] for initial benchmarking of the procedure on Imo NTs.

2.2. Optimization of empty Kohn–Sham (KS) states and Fermi golden rule optical spectra in ONETEP

The nested loops optimization of the DFT energy, density matrix [$\rho(\mathbf{r}, \mathbf{r}')$], density kernel ($K^{\alpha\beta}$) and NGWFs ($\phi_\alpha$) allows linear-scaling solution of the Kohn–Sham DFT problem for systems with a non-zero electronic BG without explicit reference to individual KS states as typical for standard plane-wave DFT. KS states can, however, be recovered from a single diagonalization of the Hamiltonian at the end of a converged calculation [139]. Although capable of accurate computation of occupied KS states, the approach nevertheless results in poor description of all but the lowest-lying unoccupied KS states since the NWGFs are optimized to describe only the occupied KS states, thence $\rho(\mathbf{r}, \mathbf{r}')$. As a result, the description of empty KS states in terms of both energy and real-space amplitude, obtained from the standard optimization of valence NGWFs, can be unsatisfactory, even omitting some higher energy (but still bound) empty KS states entirely [140].

To overcome this limitation, which prevents highly accurate calculation of KS DFT BGs, and extension towards time-dependent (TD-DDFT) or perturbative post-DFT GW approaches [141], ONETEP implements a procedure for the optimization of a second set of atom-centered conduction NGWFs (χ_α) to correctly compute empty bound KS from pre-optimized valence NGWFS (ϕ_α) and ensuing density matrix [$\rho(\mathbf{r}, \mathbf{r}')$]. The approach, described in [140], is based on the optimization of a selected number of empty KS states via nested minimization of the energy of a conduction-projected Hamiltonian (H_χ^p):

$$E = \mathrm{Tr}[M, H_\chi^p] \qquad (4)$$

with respect to the conduction NGWFs (χ_α) and related density kernel ($M^{\alpha\beta}$). H_χ^p is obtained from valence NGWFs (ϕ_α), density kernel $K^{\alpha\beta}$ and overlap matrix (S_ϕ, equation (2)):

$$H_\chi^p = (H_\chi)_{\alpha\beta} - (T^\dagger K H_\phi K T)_{\alpha\beta} + \sigma (T^\dagger K S_\phi K T)_{\alpha\beta}. \qquad (5)$$

H_χ is the unprojected conduction Hamiltonian, $T_{\alpha\beta} = \int d\mathbf{r}\, \phi_\alpha^*(\mathbf{r})\, \chi_\beta(\mathbf{r})$ is the cross-overlap between valence- and conduction-NGWFs, and σ is an energy shift applied to ensure the applicability of the procedure also to initially positive eigenvalues of the (unprojected) conduction Hamiltonian. In analogy with the optimization of the valence density kernel ($K^{\alpha\beta}$), and especially for low-energy empty KS-states with some degree of localization (i.e. occurrence of a gap in the unoccupied KS manifold), $M^{\alpha\beta}$ can be truncated via a strict distance based cutoff, allowing the procedure to scale linearly with the size of the modelled system.

Once the conduction NGWFs have been optimized, the KS-Hamiltonian can be computed and diagonalized in a joint basis encompassing both valence- (ϕ_α) and conduction- (χ_α) optimized NGWFs, yielding eigenvalues in very good agreement with the results from standard plane-wave DFT (for the occupied and optimized empty KS states). Besides, the definition of KS BGs, the optimized conduction KS states can additionally be used for calculation of optical spectra via Fermi's golden rule [140] or within the linear-response time-dependent DFT (LR-TDDFT) framework recently implemented in ONETEP [141].

As explained in [140], and considered in [114] for the Imo NTs, the convergence of this procedure can be affected by several factors such as the energy and number of the optimized conduction KS states, the similarity between valence and conduction KS states, the number of conduction NGWFs (χ_α) per atom and their localization radius.

Owing to the limitation of the adiabatic local density approximation (ALDA) for LR-TDDFT simulation of periodic semiconductors and insulators [142], optical absorption spectra were approximated on the basis of the imaginary part of the dielectric function $\varepsilon_2(\omega)$ as available in ONETEP [140]:

$$\varepsilon_2(\omega) = \frac{2e^2\pi}{\Omega\varepsilon_0} \left| \left\langle \psi_{n,k}^c | \mathbf{q} \bullet \mathbf{r} | \psi_{n,k}^v \right\rangle \right|^2 \delta(E_{n,k}^c - E_{n,k}^v - \hbar\omega) \qquad (6)$$

where v and c denote valence and conduction KS-state, respectively. $|\psi_{n,\mathbf{k}}\rangle$ is the nth KS-state, of energy $E_{n,k}$ at the kth $\mathbf{k}$-point. Ω is the simulation cell volume. $\mathbf{q}$ is the polarization direction of the incoming photon of energy $\hbar\omega$. $\mathbf{r}$ is the position operator. As explained in [140, 143–145], owing to the ill-undefined nature of $\mathbf{r}$ in periodic systems, $\varepsilon_2(\omega)$ needs to be computed via the momentum operator ($\mathbf{p}$) and then related to the position ($\mathbf{r}$) representation through corresponding commutator with the Hamiltonian. In all cases, optical spectra were computed for extended x2 supercells of the tubes based on KS-states at the Γ-point only.

Although limitations in the procedure are to be expected owing to the neglect of non-local electron–hole interactions and relaxations in the simulated spectra [142], the adopted procedure should serve as initial exploration of the role of the different composition and curvature for the optical properties of Imo NTs.

2.3. Further computational details

Simulation of the SW AlSi and SW/DW AlGe NTs were performed with the PBE functional [146]. Owing to the presence of highly polarisable methyl groups, and to test possible deficiencies of the PBE functional, SW AlSi-Me NTs were simulated with PBE, PBE with empirical dispersion corrections according to Grimme's D2 parameterization [147] (PBE-D2) and via the self-consistent dispersion functional OPTB88, chosen for the reported optimal performance in simultaneous treatment of H-bonding and methyl-group dispersion interactions [148]. In all cases, separable (Kleinman–Bylander) norm-conserving pseudopotentials [149], constructed with the opium code [150], were used.

As in [114], the adopted kinetic energy cutoff was 1000 eV and 4 (9) valence and conduction NGWFs were used for O (Al,Si) atoms. 1 NGWF was used for H atoms. In all cases, no truncation of the density kernel ($K^{\alpha\beta}$) was enforced. The localization radius for the valence (conduction) NGWFs was 8 Bohr (15 Bohr). All simulations were performed with periodic boundary conditions ensuring at least 15 Å vacuum separation between replicated images along the non-periodic directions. The conduction NGWFs optimization was performed on x2 super-cells along the tube-axis (i.e. two-fold replicas of the original minimal simulation cell) to accommodate the extended localization radius, which, together with optimization of 100 empty KS states, was necessary for sub-meV convergence of BGs and CB edges. The periodic unit for the SW-AlSi, SW-AlSi-Me, SW-AlGe and DW-AlGe NTs was the PBE-optimized one [106, 114] (SW-AlSi: 8.666 Å, SW-AlSi-Me: 8.666 Å, SW-AlGe: 8.627 Å, DW-AlGe: 8.627 Å).

Geometry-relaxations where performed via the quasi-Newton optimization scheme based on the Broyden–Fletcher–Goldfarb–Shanno (BFGS) algorithm [151].

To prevent biases due to the asymmetric distribution of the H_2O molecules inside and outside the NTs (end ensuing dipoles), vacuum-aligned KS states were obtained from 1D-periodic simulations with truncated electrostatics in the two directions perpendicular to the tube axis [152]. The adopted truncation radii (SW-AlSi: 57.2 Å, SW-AlSi-Me: 77.9 Å, SW-AlGe: 76.2 Å, DW-AlGe: 102.7 Å) were numerically checked to yield sub-meV convergence of the results. All the simulations made use of the hybrid MPI-OpenMP parallelism available in ONETEP [153].

3. Results and discussion

3.1. Structural characterization of the Imo NT-models

Investigation of Imo NTs' energy and internal strain as a function of the number of units in the Imo NTs' circumference has been the subject of intense computational and experimental research with often contrasting results [75, 83, 85–88, 104, 107–109], due to the use of different computational approximations (bulk-parameterized Hamiltonians or force fields, minimal fixed atomic basis sets, strongly reduced plane-wave energy cutoffs, semi-local or hybrid DFT functionals, neglect of solvent, fixed-cavity implicit solvation) and synthetic experimental protocols. An organized collection of the results previously published on the matter can be found in table 1 of [109].

Rather than contributing to this debate, in the absence of atomically resolved x-ray scattering or atomic force microscopy results on Imo NTs' structure (to the best of our knowledge not available in the literature), our focus is the initial exploration of the relationships between Imo NTs' composition, structure, polarization and bands alignment as well as the sensitivity of the results on the adopted DFT functional. To this end, we consider five archetypal systems of the Imo NT family, namely (i) SW AlSi ($N = 24$, **AlSi₂₄** from now), (ii) SW AlSi-Me ($N = 28$, **AlSi₂₈-Me** in the following),
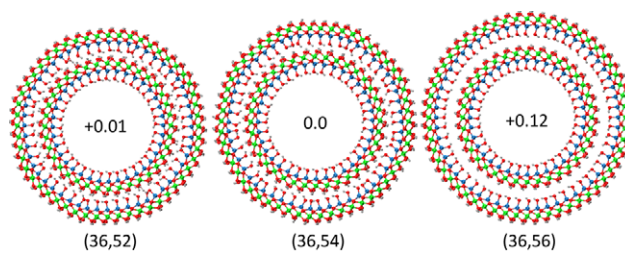
Figure 2. Front view of the optimized DW AlGe (N_{in}, N_{out}) NT models screened. The relative energy per ($Al_2GeO_7H_4$) unit (eV) is shown inside each NT-model.

(iii) SW AlSi-Me ($N = 34$, **AlSi₃₄-Me**), (iv) SW-AlGe ($N = 36$, **AlGe₃₆**), and (v) DW-AlGe ($N_{in} = 36$, $N_{out} = 54$, **DW-AlGe₃₆,₅₄**). They are shown in figure 1.

The $AlSi_{24}$ and $AlGe_{36}$ were chosen following earlier results on minimization of the (SW) AlSi (AlGe) NT-strain for 24 (36) units in the tube circumference [78, 84, 104]. AlSi₂₈-Me and AlSi₃₄-Me were selected since their optimized diameters (table 1) brackets the peak in the experimental pore-size distribution [94]. DW-AlGe₃₆,₅₄ was chosen after a minimal energy screening of different DW-AlGe NTs with smaller and larger outer NT (figure 2). It is interesting to note that, at PBE level, the energy favoured DW-AlGe₃₆,₅₄ presents an 18-unit (9-unit according to the labelling in [109]) difference between the inner and outer tubes in line with recent TB-DFT suggestions for zig-zag DW AlSi and AlGe NTs [109].

For the interested reader, table 1 reports a layer-resolved (see also figure 1) analysis of the calculated diameters for the optimized NT-models. In line with earlier ultrasoft pseudopotential plane-wave PBE-DFT results [106], the optimized outer (H_7, figure 1) diameter for the $AlSi_{24}$ (23.11 Å) and $AlGe_{36}$ (33.18 Å) NTs is in good agreement with the experimental reported values of 23 Å [75] and 30–38 Å [75, 83, 85–89, 109], respectively. The optimized outer diameter for DW-AlGe₃₆,₅₄ ($O_{6,out}$: 45.37 Å, $H_{7,out}$: 46.38 Å) also lies reasonably close to experimentally reported values for DW-AlGe NTs (40–43 Å [86, 88, 109]). DW-AlGe₃₆,₅₄ is not expected to be an energy minimum for DW-AlGe NTs [109], which explains the larger deviations from the experimentally derived diameter-range.

For the interested reader we report that the average inter-tube H-bonding distance (taking into account both $H_{7,in}$-$O_{2,out}$ and $O_{6,in}$-$H_{1,out}$ bonding patterns) is 2.23 ± 0.46 Å, with the larger standard deviation originating from a non-perfectly circular section of the NTs to maximise to the inter-tube interactions. Change from circular to hexagonal cross-section has been previously observed for SW-AlGe NTs organised in bundles [154], showing that inter-tube interactions can majorly affect the cross-sectional symmetry of SW and DW AlGe NTs.

The optimized inner diameters for the AlSi₂₈-Me (15.39 Å) and AlSi₃₄-Me (20.25 Å) are found to bracket the peak in the experimental pore distribution measured by N_2 adsorption experiments (15–20 Å [94]). Notably, the deviations between PBE, PBE-D2 and OPTB88 results of the optimized H_1-O_7 diameters for the AlSi₂₈,₃₄-Me NTs are found to be less than 0.02 Å. This result clearly indicates that the neglect (PBE)

Table 1. Average atom-resolved diameters and corresponding standard deviation (Å) for the optimized NT-models and considered DFT-functionals.

	H_1	O_2 (C_2)	Si_3 (Ge_3)	O_4	Al_5	O_6	H_7
$AlSi_{24}$ (PBE)	12.37 ± 0.02	13.25 ± 0.01	16.52 ± 0.01	17.81 ± 0.04	19.73 ± 0.02	21.91 ± 0.06	23.11 ± 0.04
$AlSi_{28}$-Me (PBE)	15.33 ± 0.03	16.10 ± 0.02	19.77 ± 0.01	21.04 ± 0.04	22.97 ± 0.01	25.15 ± 0.05	26.33 ± 0.02
$AlSi_{28}$-Me (PBE-D2)	15.35 ± 0.01	16.11 ± 0.01	19.78 ± 0.01	21.04 ± 0.04	22.97 ± 0.01	25.14 ± 0.04	26.32 ± 0.02
$AlSi_{28}$-Me (OPTB88)	15.34 ± 0.02	16.11 ± 0.01	19.78 ± 0.01	21.04 ± 0.04	22.96 ± 0.01	25.13 ± 0.04	26.33 ± 0.02
$AlSi_{34}$-Me (PBE)	20.25 ± 0.02	20.79 ± 0.01	24.45 ± 0.01	25.82 ± 0.01	27.77 ± 0.01	29.89 ± 0.01	30.92 ± 0.01
$AlSi_{34}$-Me (PBE-D2)	20.25 ± 0.02	20.78 ± 0.01	24.45 ± 0.01	25.82 ± 0.01	27.77 ± 0.01	29.89 ± 0.01	30.92 ± 0.01
$AlSi_{34}$-Me (OPTB88)	20.25 ± 0.02	20.80 ± 0.03	24.45 ± 0.01	25.82 ± 0.01	27.76 ± 0.01	29.88 ± 0.01	30.92 ± 0.01
$AlGe_{36}$ (PBE)	22.01 ± 0.02	22.79 ± 0.03	26.40 ± 0.03	27.80 ± 0.05	29.79 ± 0.02	31.95 ± 0.04	33.18 ± 0.02
DW-$AlGe_{36,54}$ (PBE)	22.08 ± 0.05	22.87 ± 0.06	26.46 ± 0.06	27.83 ± 0.09	29.81 ± 0.06	31.94 ± 0.13	33.02 ± 0.38
	(35.09 ± 0.06)	(36.19 ± 0.12)	(39.69 ± 0.10)	(41.25 ± 0.11)	(43.24 ± 0.11)	(45.37 ± 0.11)	(46.38 ± 0.55)

Note: The adopted radial labelling is reported in figure 1. For DW-$AlGe_{36,54}$ the results for the outer ($N = 54$) tube are reported in brackets.

Table 2. Computed surface dipole density (μ_σ, mD Å^{-2}) and electrostatically-derived inner (R_{in}, Å) and outer (R_{out}, Å) radii for the considered NT-models and DFT functionals.

	μ_σ (mD Å^{-2})	R_{in} (Å)	R_{out} (Å)
AlSi$_{24}$ (PBE)	34.18	4.52	13.45
AlSi$_{28}$-Me (PBE)	20.95	5.59	15.11
AlSi$_{28}$-Me (PBE-D2)	21.82	5.59	14.99
AlSi$_{28}$-Me (OPTB88)	22.69	5.59	15.11
AlSi$_{34}$-Me (PBE)	28.55	8.09	17.37
AlSi$_{34}$-Me (PBE-D2)	28.10	8.09	17.37
AlSi$_{34}$-Me (OPTB88)	29.18	8.09	17.49
AlGe$_{36}$ (PBE)	58.18	8.73	18.28
DW-AlGe$_{36,54}$ (PBE)	72.51	8.79	25.29

or inclusion (PBE-D2 and OPTB88) of dispersion interactions is effectively irrelevant for geometrical optimization of methylated Imo NTs because of the dominant contribution of the covalently bonded aluminosilicate framework to the NT diameter.

In spite of the overall acceptable agreement between computed and experimentally reported diameters, it is worth recalling that the ionic strength of the solution used for the NT synthesis is known to strongly affect the diameter of Imo AlSi NTs [80]. This makes comparison of experimental and vacuum-computed results far from conclusive. To this end, atomically resolved x-ray scattering or atomic force microscopy results would be extremely beneficial and timely for the communities with interest in Imo NTs.

3.2. Imo NTs' wall-polarization

Accumulation of negative (positive) charge on the inner (outer) tube surface, leading to a wall-polarisation of surface dipole density μ_σ, for SW AlSi and AlGe NTs has been previously considered in [106, 112]. We now analyse the extent to which μ_σ is affected by the different tube composition, diameter and number of tube walls.

Following [106], we compute μ_σ from the difference (ΔV) between the plateaus of the angularly averaged electrostatic (ionic plus Hartree) potential inside and outside the NT-cavity:

$$\Delta V = -4\pi\mu_\sigma \ln\left(\frac{R_{in}}{R_{out}}\right) \quad (7)$$

where the inner (R_{in}) and outer (R_{out}) radii of the tube are obtained from the onset of the vacuum-electrostatic plateaus, defined as the radii at which the vacuum oscillations of the local potential (V) are smaller than an arbitrary (5×10^{-3} eV) threshold. For the adopted sign convention, positive μ_σ values indicate accumulation of negative (positive) charge-density at the inner (outer) surface of the NTs.

Table 2 reports the computed μ_σ and $R_{in/out}$ for all the considered cases. Not unexpectedly given the established numerical equivalence between the ONETEP approach and plane-wave DFT [121], the computed μ_σ for AlSi$_{24}$ (34.18 mD Å^{-2}) and AlGe$_{36}$ (58.18 mD Å^{-2}) is in very good agreement with previous ultrasoft pseudopotential plane-wave PBE-DFT results (AlSi$_{24}$: 30 mD Å^{-2}, AlGe$_{36}$: 60 mD Å^{-2} [106]).

The substitution of inner hydroxyl groups (–OH) with methyl (–CH$_3$) functionalities in AlSi$_{28,34}$-Me is found to leave the direction of wall polarization unperturbed, whilst reducing the magnitude the simulated μ_σ. The decrease for AlSi$_{28}$-Me (-38.6%) is larger than for AlSi$_{34}$-Me (-16.5 %). Further simulation of AlSi$_{24}$-Me, to be reported elsewhere [155], confirms the reduction of the wall-polarization to be mainly due to the presence of the less polar methyl groups. With maximum deviations smaller than 8% (AlSi$_{28}$-Me at PBE and OPTB88 level), the PBE, PBE-D2 and OPTB88 results suggest a very weak dependence of the computed μ_σ on the use or neglect of dispersion interactions. Given the similarity between the optimized geometries (table 1) the computed differences stem from a different decay of the (occupied) KS-states inside and outside the NT-cavity, leading to different potential steps (ΔV) in equation (7).

Encapsulation of two AlGe NTs in DW-AlGe$_{36,54}$ is computed to noticeably increase (+24.6 %), albeit not double, μ_σ with respect to the SW-AlGe$_{36}$ value. Overall these results indicate that by tuning Imo NTs composition and diameter (i.e. curvature), control of the wall-polarization (thence affinity for electro-positive and negative species) can be readily achieved. Whereas methylation of Imo NTs is found to decrease the wall-polarization, creation of DW systems results in larger μ_σ.

3.3. Imo NTs' electronic structure and absolute band alignment

For an insulator to be viable as a PC for a given reaction, the position of its VB and CB edges with respect to the h- and e-acceptor levels of the reactants, and effective e*-h separation, are of utmost importance [1–14]. To begin assessing the potential of Imo NTs as possible photocatalysts, here we investigate the absolute vacuum alignment of the isolated NTs' VB and CB edges and their real-space distribution. Furthermore, the vacuum-aligned Imo NT band edges are discussed with respect to recent combined x-ray photoemission spectroscopy, optical spectroscopy and electrostatically embedded DFT results for the bulk-phases of two archetypal photocatalysts, namely anatase and rutile TiO$_2$ [156].

We recall that, qualitatively, for energetically viable transfer of excited e* from a PC to a reactant, the empty e-acceptor state of the reactant needs to be *lower* in energy than the CB-edge of the PC. Conversely, for energetically viable h-transfer from a PC to a reactant, the highest-energy occupied h-acceptor state of the reactant needs to be *higher* in energy than the VB-edge of the PC [1–13].

We also note that, owing to the use of semi-local approximations to the exchange component of the adopted PBE(-D2) and OPTB88 DFT-functionals [146, 148], overestimation (underestimation) of the computed energy of the VB (CB) edge, leading to an overall underestimation of the BG, is to be expected [157–162]. Accordingly, the computed Imo NTs VB and CB edges should be taken as upper and lower boundary of the Imo NTs' band edges, respectively. The following analysis neglects also the role of PC-reactants (medium) interfacial relaxations, which may affect the combined system electrostatics and, accordingly, the band alignment. These effects
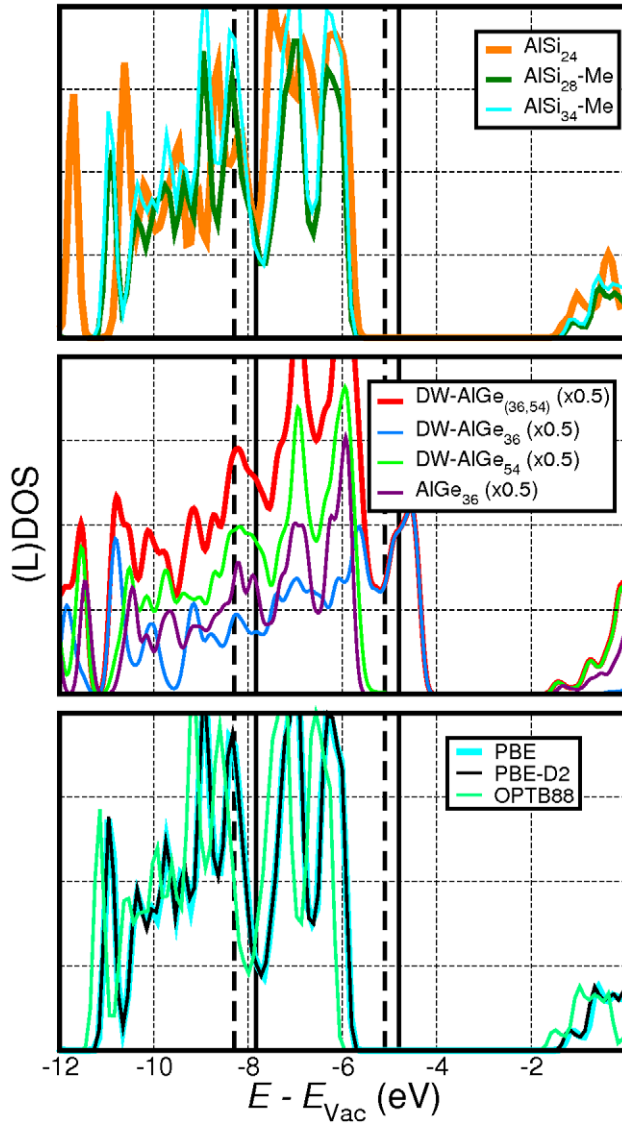
Figure 3. Vacuum-aligned DOS and tube-projected LDOS for the considered Imo NTs and DFT-functionals. The VB and CB edges for bulk anatase (dotted) and rutile (continuous) TiO$_2$, obtained from addition of the experimental optical gap to the computed ionization potential [156], are marked with black vertical lines.

Table 3. Vacuum-aligned VB and CB edges (eV), and computed BG (eV) for the considered Imo NTs and DFT-functionals.

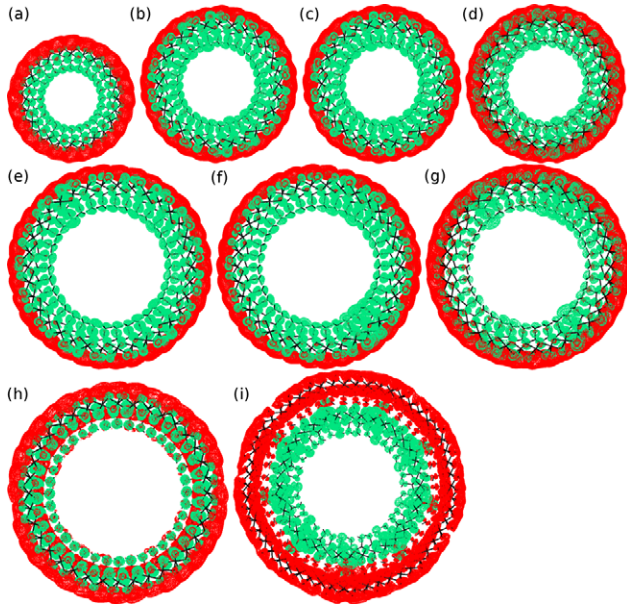|	VB (eV)	CB (eV)	BG (eV)
AlSi$_{24}$ (PBE)	−5.80	−1.36	4.44
AlSi$_{28}$-Me (PBE)	−5.97	−1.22	4.75
AlSi$_{28}$-Me (PBE-D2)	−5.96	−1.24	4.72
AlSi$_{28}$-Me (OPTB88)	−6.21	−1.54	4.67
AlSi$_{34}$-Me (PBE)	−5.97	−1.23	4.74
AlSi$_{34}$-Me (PBE-D2)	−5.97	−1.26	4.71
AlSi$_{34}$-Me (OPTB88)	−6.24	−1.56	4.68
AlGe$_{36}$ (PBE)	−5.74	−1.39	4.35
DW-AlGe$_{36,54}$ (PBE)	−4.30	−1.49	2.81
DW-AlGe$_{36,54}$ (inner NT)	−4.30	−0.93	3.37
DW-AlGe$_{36,54}$ (outer NT)	−4.92	−1.49	3.43
Rutile TiO$_2$[a]	−7.83	−4.80	3.03
Anatase TiO$_2$[a]	−8.30	−5.10	3.20

[a] Reference [156].

for the different DFT-functionals, highlights the negligible role played by dispersion interactions in the simulation of methylated Imo NT BGs.

In line with previous PBE results [103, 106] AlGe$_{36}$ is also computed to be an insulator with a 4.35 eV BG. Notably, the DW-AlGe$_{36,54}$ BG (2.81 eV) is substantially smaller (−1.54 eV) than for AlGe$_{36}$. As indicated by the inner- and outer-tube resolved local DOS (LDOS [164]) in figure 3, this result stems from the mutual polarization of the inner and outer tubes, leading to an upward (downward) shift of the inner (outer) tube electronic bands. Although the calculated BG for DW-AlGe$_{36,54}$ is likely underestimated due the limitations of the PBE functional, the computed reduction in BG going from AlGe$_{36}$ to DW-AlGe$_{36,54}$ should be, at least qualitatively, significant.

Turning to the vacuum band alignment for the Imo NTs, at PBE-level the lowest (−5.97 eV) and highest (−4.30) VB edge is found for AlSi$_{28/36}$-Me and DW-AlGe$_{36,54}$, respectively. Instead, the lowest (−1.49 eV) and highest (−1.22/−1.23) CB edge is found for DW-AlGe$_{36,54}$ and AlSi$_{28/34}$-Me, respectively. Charge depletion by the methyl group (0.3 e/CH$_3$) leads to nearly 0.2 eV lowering (0.15 eV increase) of the AlSi$_{28/36}$-Me VB (CB) edge with respect to AlSi$_{24}$. Work is in progress to investigate whether this mechanism is present also in methylated hybrid Si/Ge Imo NTs [96].

Comparison between the band edges of SW-AlGe$_{36}$ and DW-AlGe$_{36,54}$ reveals that encapsulation of AlGe NTs causes a large (1.44 eV) upward shift of the VB-edge with simultaneous, but smaller, lowering (0.1 eV) of the CB-edge, leading to a marked narrowing (−1.54 eV) of the computed BG.

On a specialist note, and in contrast with the results for the optimized geometries and BGs, the inclusion of dispersion interactions in the functional is found to affect (up to nearly 0.3 eV) the absolute alignment of the VB and CB edges. It thus turns out that some care should be exerted when comparing vacuum-aligned band edges obtained with non-local (PBE) or self-consistent dispersion corrected (OPTB88) DFT-functionals.

will be considered in the next section for model NT-H$_2$O interfaces.

Figure 3 reports the vacuum-aligned density of states (DOS) for the considered Imo NTs. The computed band edges and BGs are collected in table 3. We note that the computed BG for AlSi$_{28}$-Me and AlSi$_{34}$-Me (4.67–4.75 eV depending on the adopted functional) is 0.23–0.31 eV larger than for AlSi$_{24}$. Thus, in spite of substitution of more polar hydroxyls by less polar methyl units, the Imo NT BG increases upon methylation of the cavity. Mulliken population analysis [163] for AlSi$_{28/34}$-Me indicates that the modelled BG opening is accompanied by a non-negligible charge transfer of 0.30 ± 0.01 e/CH$_3$, depending on the adopted functional, from the gibbsite (aluminium hydroxide) backbone to the methyl groups. Thus, we compute the methyl groups in the Imo NTs to be negatively charged. On a more specialist note, the marginal deviations (<0.08 eV) between the computed BG of AlSi$_{28/34}$-Me

Figure 4. Front view of the VB (green) and CB edge (red) separation for the considered Imo NTs and DFT functionals. (a) $AlSi_{24}$ (PBE), (b) $AlSi_{28}$-Me (PBE), (c) $AlSi_{28}$-Me (PBE-D2), (d) $AlSi_{28}$-Me (OPTB88), (e) $AlSi_{34}$-Me (PBE), (f) $AlSi_{34}$-Me (PBE-D2), (g) $AlSi_{34}$-Me (OPTB88), (h) $AlGe_{36}$ (PBE), (i) DW-$AlGe_{36,54}$ (PBE). The structures in (a)-(h) are displayed according to their relative size (table 1). For more compact representation, the structure in (i) has been scaled down by a factor 1.5. The six lowest-energy occupied and highest-energy empty KS-states have been plotted for the VB and CB edge in (a)–(h), respectively. For DW-$AlGe_{36,54}$, thirty two (sixteen occupied, sixteen empty) frontier KS-states have been used.

Previous DFT simulation of AlSi and AlGe Imo NTs have revealed an intriguing real-space separation of the VB and CB edges [106, 107], which may be beneficial for e*-h separation. The extent to which this peculiar property is affected by methylation or creation of DW-AlGe NTs has to date not been investigated. Our simulations suggest that the separation in real-space between the VB and CB edges is qualitatively unaffected by methylation or the choice of the DFT-functional (figure 4). Notably, and in line with the tube-projected and layer-resolved results for DW-$AlGe_{36,54}$ (figure 3 and the supporting information at (stacks.iop.org/JPhysCM/28/074003/mmedia)), the VB and CB edge of the DW-$AlGe_{36,54}$ are found to be localised on different tubes, with the VB (CB) edge on the inner (outer) tube, leading to the intriguing possibility of e*-h relaxation on different faces of different AlGe NTs.

Consistent with the real-space distribution of the VB and CB edges in figure 4, layer-resolved, NGWF-projected [164], analysis of the computed DOS (LDOS, see supporting information) indicates major contributions of the O_2/O_4 (H_7) layers to the VB (CB) edge of $AlSi_{24}$. Similarly, the VB (CB) edge of $AlSi_{28,34}$-Me is found to be dominated by C_2/O_4 (H_7) layers. DW-$AlGe_{36,54}$ is more peculiar with leading contributions to the CB and VB edges from inner O_2/O_4 and outer Al_5/H_7 layers, respectively. With larger contributions from the Ge_3 (O_6) layer to the CB (VB) band edges, the real-space separation of the latter for $AlGe_{36}$ is found to be less pronounced than for the other NTs.
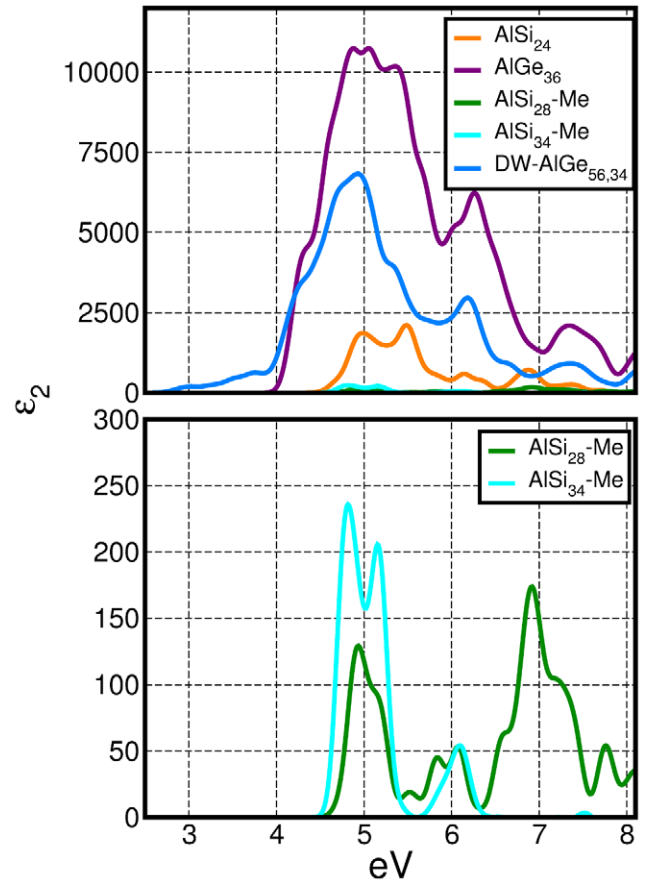
Figure 5. Top: calculated imaginary component of the dielectric function (ε_2) for the considered Imo NTs. To facilitate comparison, each spectrum has been normalized to the total number of Imo units (*N*) present in the NT-models. Bottom: close up on the $AlSi_{28}$-Me and $AlSi_{34}$-Me results.

Finally, we note that the PBE, PBE-D2 and OPTB88 layer-resolved LDOS for $AlSi_{28}$-Me and $AlSi_{34}$-Me are effectively undistinguishable (see supporting information), which demonstrates a marginal role of inclusion of dispersion corrections for the modelled LDOS in methylated AlSi-Me NTs.

3.4. Comparison between Imo NTs and TiO₂ vacuum-aligned band edges

To better put these results into wider context, figure 3 and table 3 report vacuum-aligned band edges also for rutile and anatase TiO_2 [156], whose mixture is known to lead to effective water photolysis [165]. By comparing the relative energy of TiO_2 and the Imo NTs' band edges, we begin to estimate the NTs' possible increased or reduced drive towards H_2O reduction or oxidation, neglecting any interfacial effects.

The vacuum-aligned VB-edges of the Imo NTs are at least 1.86 eV (2.33 eV) higher than rutile (anatase) VB-edge. Neglecting any electron transfer kinetics consideration, this result suggests a lower H_2O photo-oxidation propensity for Imo NTs with respect to TiO_2. Additionally, the CB-edge for the Imo NTs is at least $+3.31$ eV and $+3.61$ eV higher in energy than the rutile and anatase, respectively. Again
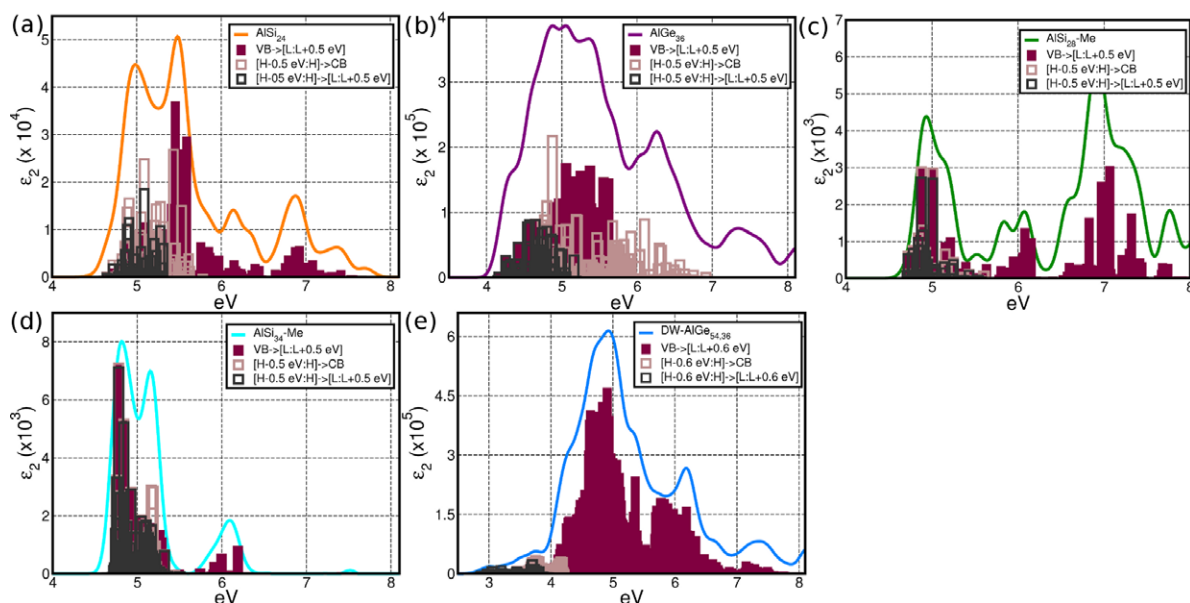
Figure 6. KS-state resolved analysis of the largest contributions to the low-energy values of ε_2 for (a) AlSi$_{24}$, (b) AlGe$_{36}$, (c) AlSi$_{28}$-Me, (d) AlSi$_{34}$-Me, (e) DW-AlGe$_{36,54}$. H (HOMO) and L (LUMO) indicate the highest-energy occupied and lowest-energy empty KS-state, respectively. The VB and CB edges include the KS-states within 0.5 eV (0.6 eV for DW-AlGe$_{36,54}$) from H (VB) and L (CB), respectively. Excitations between VB and CB edges are marked as '[H-0.5 eV:H] $\rightarrow$ [L:L + 0.5 eV]'. Excitations from the VB-edge to the whole CB and from the whole VB to the CB-edge are marked as '[H-0.5 eV:H] $\rightarrow$ CB' and 'VB $\rightarrow$ [L:L + 0.5 eV]', respectively.

neglecting any kinetics consideration, this suggests a higher drive for H$_2$O photo-reduction by Imo NTs in comparison to TiO$_2$. This analysis rests on the assumption that the NT wall-polarization has a negligible role in shifting the H$_2$O acceptor and donor states. In the next section we explore this assumption and the extent to which the NT wall-polarisation shifts the electronic states of interacting molecules.

Finally, while detrimental to their possible use as photo-oxidants, the rather high-energy VB-edges of the Imo NTs, lying between −5.97 eV (AlSi$_{28/34}$-Me) and −4.30 eV (DW-AlGe$_{36,54}$), suggest that grafting a molecular or nanoparticle PC to Imo-NTs may result in a rewarding strategy towards enhanced e*-h separation by promoting h-transfer and relaxation from the grafted PC onto the NT.

3.5. Imo NTs' optical absorption

In spite of the growing research interest in Imo NTs, to date their optical absorption properties have not been very extensively studied. To the best of our knowledge, the only published UV–visible absorption spectrum for Imo NTs is the one reported in [78], obtained for the synthetic solution into which AlGe NTs were made, that is, without any previous separation of the Imo NTs from the unreacted precursors and possible photoactive side-products.

We now present simulated optical spectra of the (isolated and neutral) Imo-NTs in an attempt to contribute to characterization of their optical properties. Figure 5 shows the computed imaginary component of the dielectric function (ε_2, see equation (6)) for the considered NT models. Larger values of ε_2 indicate a larger absorbance of the system. Owing to our interest in assessing possible differences between the different Imo NTs, and in order to maintain reasonable the
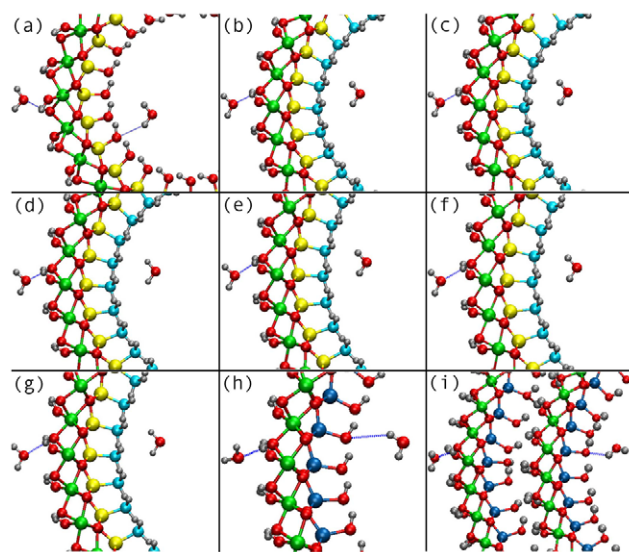
Figure 7. Close up of the optimized geometry of the considered 2H$_2$O@Imo NTs models for the DFT-functionals used. (a) AlSi$_{24}$ (PBE), (b) AlSi$_{28}$-Me (PBE), (c) AlSi$_{28}$-Me (PBE-D2), (d) AlSi$_{28}$-Me (OPTB88), (e) AlSi$_{34}$-Me (PBE), (f) AlSi$_{34}$-Me (PBE-D2), (g) AlSi$_{34}$-Me (OPTB88), (h) AlGe$_{36}$ (PBE), (i) DW-AlGe$_{36,54}$ (PBE). The shortest H$_2$O-NT H-bonding distances (see also table 4) are highlighted by dotted lines. Same atom-colour labelling as in figure 1.

computational cost, all the spectra were simulated at PBE level. We recall that given the limitations of the adopted DFT-functional and approximations for the evaluation of optical spectra (section 2) expectations are that the energy of the optical transitions will be underestimated.

The experimental spectra for the AlGe NTs' synthetic solution show a main absorbance peak at 6.2 eV with a broad shoulder in the 5–5.4 eV range, and a well-defined secondary

Table 4. The shortest H_2O-NT (H-bond) distances (d, Å) and Mulliken charges (q, e) for the H_2O molecule inside (outside) the considered NT-models for the different DFT-functionals used.

	d (Å)	q (e)
$AlSi_{24}$ (PBE)	2.38 (2.09)	−0.01 (+0.05)
$AlSi_{28}$-Me (PBE)	2.32 (2.08)	+0.01 (+0.05)
$AlSi_{28}$-Me (PBE-D2)	2.32 (2.08)	+0.01 (+0.05)
$AlSi_{28}$-Me (OPTB88)	2.40 (2.00)	0.00 (+0.07)
$AlSi_{34}$-Me (PBE)	2.34 (2.10)	+0.01 (+0.04)
$AlSi_{34}$-Me (PBE-D2)	2.28 (2.20)	+0.01 (+0.04)
$AlSi_{34}$-Me (OPTB88)	2.31 (2.13)	0.00 (+0.05)
$AlGe_{36}$ (PBE)	2.49 (2.09)	0.00 (+0.02)
$AlGe_{36,54}$ (PBE)	2.09 (2.11)	−0.01 (+0.05)

peak at 3.9 eV [78]. Given the expected underestimation of the $AlGe_{36}$ BG (section 3.3) we associate the simulated main 5 eV peak (figure 5) to the experimental 6.2 eV signature. Analysis of the optical matrix elements (figure 6) indicates that transition involving deep VB and CB KS-states are optically active and contribute significantly to the modelled spectrum. The lower energy absorbance shoulder (associated to the 5–5.4 eV experimental feature) is seen to originate from transitions involving the VB and CB edges, which, as shown in figure 4, are separated on different sides of the NT cavity. We speculate that these optically active inside–outside charge-transfer excitations may be beneficial for effective e*-h separation because recombination would have to occur in the direction against the wall-polarization (table 2).

The simulations for the defect-free $AlGe_{36}$ model do not present any secondary absorbance peak detached from the main one. Being at lower energy than the underestimated PBE-gap (4.35 eV, table 3), it has been suggested that the experimental 3.9 eV peak may be due to excitonic effects in AlGe NTs [78, 106], which cannot be captured by single-electron approximations to the optical spectra [142] as used here. Besides obvious limitations of equation (6), the disagreement between experiment and simulations could also stem from the fact that the experimental 3.6 eV peak is due to absorbance by point-defects (known to exist in AlSi NTs [113]), the tube-terminations (which have not been accounted for in this work) or to the presence of unreacted precursors, photoactive side-products or NT-aggregates in the synthetic solution monitored in [78]. Work is in progress to investigate these aspects.

Comparison of the calculated spectra, normalized by the number of Imo units present in the NT, indicates that optical absorbance of $AlGe_{36}$ (DW-$AlGe_{36,54}$) is nearly six (four) times larger than $AlSi_{24}$, with the absorbance of methylated $AlSi_{28}$-Me and $AlSi_{34}$-Me being the lowest (over forty five times smaller than $AlGe_{36}$). That is, the modelled absorbance per Imo unit is found to decrease going from SW $AlGe_{36}$ to DW-$AlGe_{36,54}$, SW $AlSi_{24}$, and methylated $AlSi_{28}$-Me and $AlSi_{34}$-Me NTs. Although, the low-energy ε_2 peak is found to weakly depend on the NT composition, being bracketed between 4.83 eV ($AlSi_{34}$-Me) and 4.94 eV ($AlSi_{24}$), the appearance of an absorbance shoulder in the 3–4 eV range for DW-$AlGe_{36,54}$ indicates the creation of DW NTs is effective
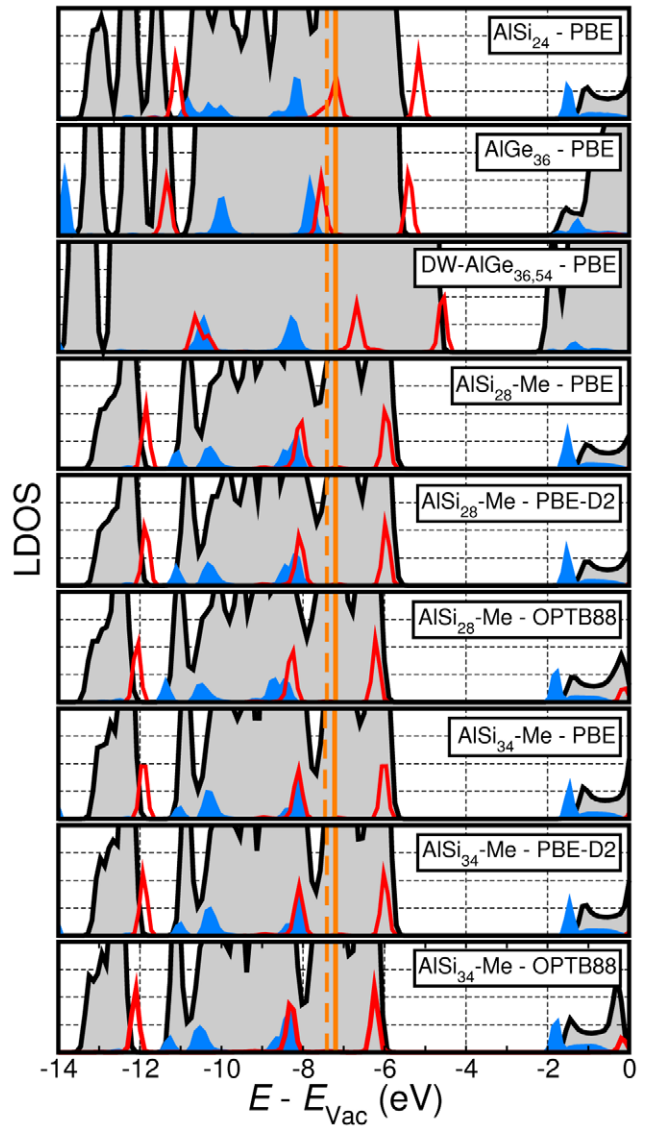
Figure 8. NT (filled grey) and H_2O-resolved, vacuum-aligned, LDOS for the optimized $2H_2O@Imo$ NT systems and adopted DFT-functionals. The inner H_2O and outer H_2O PDOS are displayed in red and blue, respectively. The energy of the HOMO level of one isolated H_2O molecule according to PBE and PBE-D2 (−7.200 eV), and OPTB88 (−7.413 eV) are marked by orange vertical continuous (PBE, PBE-D2) and dotted (OPTB88) lines, respectively. In accordance with the literature [167], the PBE (PBE-D2) and OPTB88 LUMO-level for one isolated H_2O molecule is above the 0 eV vacuum-level (PBE(-D2): +0.629 eV, OPTB88: +0.262 eV, not shown in the graph).

in introducing lower-energy (near-UV) absorption. Notably, the lower-energy absorbance shoulder of DW-$AlGe_{36,54}$ is dominated by inter-tube charge-transfer excitations (figure 6), which may be extremely effective for e*-h separation because of the larger separation between inner and outer NTs ($H_{7,in}$-$H_{1,out}$: 2.07 Å, $H_{1,in}$-$H_{7,out}$: 24.03 Å, see table 1).

Finally, the optical matrix elements for transitions involving states at the VB and CB edges of the methylated $AlSi_{28,34}$-Me NTs are found to dominate the main absorbance peak (figure 6). Thus, contrary to $AlSi_{24}$ and $AlGe_{36}$ (DW-$AlGe_{36,54}$), the optical absorbance of the AlSi-Me NTs turns out to be

primarily due to transitions between states localised on different sides of the NT cavity.

3.6. H2O at Imo NTs

Suitable electronic alignment between the PC band-edges and the reactant e (h) acceptor state(s) is crucial for viable photo-induced e (h) transfer from the PC to the reactant. As a result, PC band engineering to match a given reactant e (h) acceptor states continues to be the subject of intense research [1–14].

Two concepts, to the best of our knowledge substantially less explored, are whether by engineering of the electrostatics of nano-cavities (i) reactants can be forced to match the band edge of a (polarizing) PC and (ii) nano-confinement of PCs and reactants of expectedly different polarizability in a polarizing environment can be used to tailor electronic line-ups between a prospect PC and a given reactant. With inner diameters ranging from 12 Å up to 22 Å (table 1), and markedly different electrostatic environments on either sides of the NT cavity (table 2), Imo NTs emerge as an ideal system to start exploring these concepts. To this end, we investigate the effect of the NTs' wall-polarization on H_2O molecules interacting with inner and outer surface of the considered Imo NTs (figure 7).

Table 4 reports the optimized shortest distances between the H_2O molecule and the NT hosts, together with the computed Mulliken [163] charges. The noticeably longer ($\geqslant +0.29$ Å) distances of the inner H_2O with respect to the outer H_2O for the SW hydroxylated $AlSi_{24}$ and $AlGe_{34}$ NTs indicate weaker H-bonding at the electronegative (table 2) NT-cavity. Conversely, the deviations between outer and inner H-bonding for the DW-$AlGe_{36,54}$ NT (0.02 Å) are found to be negligible. Thus, H-bonding of H_2O at the NT cavity turns out to be governed by a subtle interplay between the NT-polarization and curvature, with smaller inside/outside differences for less curved (DW-$AlGe_{36,54}$) substrates.

Methylation of the NT-cavity for $AlSi_{28,34}$-Me is found to minimally affect (± 0.01 Å) the outer H-bonding distance. Not unexpectedly given the different treatment of dispersion interactions, the inner H_2O-NT distance is found to be sensitive (up to ± 0.08 Å differences) to the adopted DFT-functional. It is interesting to note that the deviations between PBE, PBE-D2 and OPTB88 results are different for $AlSi_{28}$-Me and $AlSi_{34}$-Me, indicating that both the cavity polarization (table 2) and dispersion interactions jointly affect the adsorption of H_2O on the NT inner methylated surface.

In all cases, interaction of the H_2O molecule with the outer hydroxylated surface is found to be accompanied by small, yet non-negligible, electronic charge depletion, leading to a partially positive (+0.02/+0.07 e) adsorbed H_2O. Conversely, negligible charge transfer ($\leqslant 0.01$ e) is modelled for the inner H_2O molecule.

H_2O adsorption on the outer surface of a carbon nanotube (CNT) has been recently shown to lead to negligible ($<10^{-4}$ e/molecule) electron transfer from H_2O to the CNT [166]. Thus, contrary to this CNT case, and likely due to the presence of H-bonding not offered by the CNT, we find the interactions of H_2O and Imo-NTs to be instead accompanied by

a small charge transfer. Although simulation of periodically repeated small H_2O/NT rings (as considered here) may lead to overestimation of the charge-transferred [166], the trends among the Imo NTs considered should be robust.

Turning to the effect of NT wall-polarization on interacting H_2O molecules, figure 8 reports vacuum-aligned LDOS for the considered H_2O@Imo NT systems. Consistent with the more electronegative (positive) potential at the inner (outer) surface of the NTs, and regardless of the NT composition and adopted DFT-functional, the HOMO of the inner H_2O molecule is invariably shifted (by up to roughly 3 eV for $AlSi_{24}$ and DW-$AlGe_{36,54}$) to higher energies with respect to the outer H_2O molecule. Upward (downward) shift is computed also for the LUMO of the inner (outer) H_2O molecule. These results demonstrate that the NT wall-polarization can induce major changes in the electronic alignment of adsorbed H_2O. We speculate that qualitatively similar results may be found also for other adsorbates.

Comparison of the HOMO-energy between the adsorbed molecules and one isolated H_2O molecule in vacuo (figure 8) indicates that, depending on the adsorption side, and neglecting any electron transfer kinetics consideration, oxidation of the inner (outer) H_2O should be energetically favoured (disfavoured) over the same process in vacuo because of the higher (lower) HOMO. Interestingly, owing to the NT wall-polarization and outer electropositive environment, the LUMO-level of the outer H_2O molecule is brought below the vacuum-level (0 eV), leading to a positive electron affinity (EA) for the adsorbed H_2O molecule in stark contrast with the negative EA for isolated H_2O [167].

The PBE alignment between the inner H_2O HOMO (outer H_2O LUMO) and the NT top VB (bottom CB) edge is compatible with photo-oxidation (photo-reduction) of the inner (outer) H_2O by $AlSi_{24}$. With a HOMO-energy higher than the NT top VB-edge, energetically viable photo-oxidation of the inner H_2O molecule by the NT is modelled also for $AlGe_{36}$ and DW-$AlGe_{36,54}$. Conversely, owing to a LUMO-energy higher than the NT bottom CB-edge, photo-reduction of the outer H_2O molecule by the $AlGe_{36}$ ($AlGe_{36,54}$) lowest-energy CB-states is computed to be energetically unviable. However, population of deep (higher energy) CB-states via active (figure 6) optical excitations could be energetically compatible with photo-reduction of the outer H_2O molecule. The competition between kinetics of CB e*-relaxation and NT → H_2O e*-transfer will be the subject of future investigations.

Regardless of the adopted functional, electronic alignment suitable to photo-reduction of the outer H_2O molecule (LUMO energy lower than bottom CB-edge) is computed also for $AlSi_{28,34}$-Me. Conversely, the alignment between the inner H_2O HOMO and the $AlSi_{28,34}$-Me top VB-edge is less favourable than for non-methylated $AlSi_{24}$, at least for the considered optimized geometries. In spite of this, optically active (figure 6) excitations from deep VB-states and creation of holes deep in the VB could nevertheless promote photo-oxidation of the inner H_2O molecule by the methylated $AlSi_{28,34}$-Me NTs. Future work will consider the competition between kinetics of VB h-relaxation and NT → H_2O h-transfer.

Several notes of caution are in place. First, the present analysis neglects any consideration of the electron (hole) transfer kinetics [168]. Thus, even if the modelled electronic alignments are appealing, the electron (hole) transfer kinetics may be impractically slow. Second, the analysis is based on the optimized geometries of highly idealised models in vacuo, which may not fully capture the real photo-electro-chemistry of the defective and solvated NTs. Depending on the polar nature of the medium interacting with the NTs [169–172], the wall-polarization may be differently screened, leading to non-negligible deviations from the computed shifts for the H_2O HOMO and LUMO levels. Third, the role of temperature-induced fluctuations [173–176] for the dynamic NTs-H_2O electronic line-ups, which may well be non-negligible, has also been neglected. Fourth, the discussion presented is based on the use of KS-states which, apart from the highest-energy occupied one and neglecting functional limitations, ultimately do not have strong physical significance in terms of molecular acceptor and donor states [177–180]. Work is in progress to advance along these lines. In spite of these objective limitations, partially or completely shared with most of the current DFT-based theoretical production on PC materials [20–27], we hope this initial contribution will be effective in stimulating further input by the scientific community with interest in photocatalysis and photocatalytic materials.

4. Conclusion

Simulation with three different DFT-functionals (PBE, PBE-D2, OPTB88) of SW-AlSi$_{24}$, SW-AlSi$_{28}$-Me, SW-AlSi$_{34}$-Me, SW-AlGe$_{36}$ and DW-AlGe$_{36,54}$ Imo NTs either isolated or interacting with two H_2O molecules indicates that:

(i) by controlling the Imo NT composition and curvature, the NT wall-polarization can be changed by nearly a factor of four with the lowest value (20.95 mD Å^{-2}) for SW AlSi$_{28}$-Me and the largest value for DW-AlGe$_{36,54}$ (72.51 mD Å^{-2}). Regardless of the NT composition and SW or DW nature, the NT inner surface is always more electronegative than the outer surface. The computed wall-polarization for methylated AlSi$_{28}$-Me and AlSi$_{34}$-Me NTs is found to be weakly (~8%) affected by the adopted DFT-functional.

(ii) All the considered NTs are insulators with computed (likely underestimated by the functionals used) BGs ranging from 2.81 eV (DW-AlGe$_{36,54}$) to 4.75 eV (AlSi$_{28}$-Me). Use of PBE, PBE-D2 or OPTB88 is found to minimally (≤0.08 eV) affect the computed BGs for the methylated NTs.

(iii) Regardless of the NT composition and curvature, SW or DW nature, and adopted DFT-functional, the VB (CB) edge is consistently modelled to be mostly localised at the NT inner (outer) surface.

(iv) The absolutely vacuum-aligned NT VB edges are noticeably high in energy (>-5.97 eV), which suggests possible strong hole-scavenging propensity.

DW-AlGe$_{36,54}$ is found to have the highest VB-edge (-4.30 eV).

(v) The absolutely vacuum-aligned NT CB edges are also found to be remarkably high in energy (>-1.49 eV), which anticipates possible marked photoreduction propensity. SW AlSi$_{28}$-Me is found to have the highest CB-edge (-1.22 eV).

(vi) By comparison to rutile and anatase TiO_2, the Imo NTs have noticeably higher VB (up to $+4.0$ eV) and CB-edges (up to $+3.6$ eV).

(vii) Contrary to the results for the wall-polarization and BGs, the absolute band-alignment of the AlSi$_{28,34}$-Me NTs is found to be non-negligibly (~0.3 eV) affected by the choice of the functional, with OPTB88 yielding lower VB-edges than PBE and PBE-D2. Accordingly, care should be exerted when comparing vacuum-aligned band edges obtained with non-local (PBE) or self-consistent dispersion (OPTB88) DFT-functionals.

(viii) The optical activity of SW-AlGe$_{36}$ and DW-AlGe$_{36,54}$ NTs is noticeably (nearly six- and four-fold, respectively) larger than SW-AlSi$_{24}$ NTs, which in turn have substantially (nearly eight-fold) larger UV absorbance than methylated SW-AlSi$_{28,34}$-Me NTs. This analysis has been performed for isolated, neutral NT-models.

(ix) The NT wall-polarization is found to markedly affect the electronic alignment of H_2O molecules interacting with either surface of the NTs. The computed alignment of the CB bottom edges suggests energetically viable photo-reduction of H_2O at the outer surface of all the considered NT models apart from DW-AlGe$_{36,54}$. Photo-oxidation of H_2O inside the NT-cavity by the top VB edge is modelled to be energetically favoured for all the non-methylated NTs (SW AlSi$_{24}$, SW AlGe$_{36}$, DW-AlGe$_{36,54}$). This analysis neglects any electron transfer kinetics consideration and the role of solvent and temperature effects in altering the H_2O-NT relative band-alignment.

References

[1] Hoffmann M R, Martin S T, Choi W Y and Bahnemann D W 1995 *Chem. Rev.* **95** 69

[2] Hagfeldt A and Grätzel M 1995 *Chem. Rev.* **95** 49

[3] Fox M A and Dulay M T 1993 *Chem. Rev.* **93** 341

[4] Yang Y, Zhong H and Tian C X 2011 *Res. Chem. Intermediat.* **37** 91

[5] Rauf M A and Ashraf S S 2009 *Chem. Eng. J.* **151** 10

[6] Fujishima A, Zhang X T and Tryk D A 2008 *Surf. Sci. Rep.* **63** 515

[7] Chong M N, Jin B, Chow C W K and Saint C 2010 *Water Res.* **44** 2997

[8] Ahmed S, Rasul M G, Martens W N, Brown R and Hashib M A 2010 *Desalination* **261** 3

[9] Maeda K and Domen K 2010 *J. Phys. Chem. Lett.* **1** 2655

[10] Kitano M and Hara M 2010 *J. Mater. Chem.* **20** 627

[11] Ji P F, Takeuchi M, Cuong T M, Zhang J L, Matsuoka M and Anpo M 2010 *Res. Chem. Intermediat.* **36** 327

[12] Hernandez-Alonso M D, Fresno F, Suarez S and Coronado J M 2009 *Energy Environ. Sci.* **2** 1231

[13] Morris A J, Meyer G J and Fujita E 2009 *Acc. Chem. Res.* **42** 1983

[14] Hagfeldt A and Gratzel M 2000 Molecular photovoltaics *Acc. Chem. Res.* **33** 269

[15] Sastre F, Fornes V, Corma A, and García H 2011 Selective *J. Am. Chem. Soc.* **133** 17257

[16] Ciamician G 1912 The photochemistry of the future *Science* **36** 385

[17] Tong H, Ouyang S, Bi Y, Umezawa N, Oshikiri M and Ye J 2012 *Adv. Mater.* **24** 229

[18] Djurišić A B, Leunga Y H and Ng A M C 2014 *Mater. Horiz.* **1** 400

[19] Weng B, Liu S, Tang Z-R and Xu Y-J 2014 *RSC Adv.* **4** 12685

[20] Sato J, Kobayashi H and Inoue Y 2003 *J. Phys. Chem.* B **107** 7970

[21] Tong H, Ouyang S, Bi Y, Umezawa N, Oshikiri M and Ye J H 2012 *Adv. Mater.* **24** 229

[22] Nashed R, Ismail Y and Allam, N K 2013 *J. Renew. Sus. Chem.* **5** 022701

[23] Liu L-M, Crawford P and Hu P 2009 *Prog. Surf. Sci.* **84** 155

[24] Li Y-F, Aschauer U, Chen J and Selloni A 2014 *Acc. Chem. Res.* **47** 3361

[25] Di Valentin C and Pacchioni G 2014 *Acc. Chem. Res.* **47** 3233

[26] Dong S, Feng J, Fan M, Pi Y Q, Hu L, Han X, Liu M, Sun J and Sun J 2015 *RSC Adv.* **5** 14610

[27] Bhatt M D and Lee J S 2015 *J. Mater. Chem.* A **3** 10632

[28] Jung H S, Hong Y J, Li Y, Cho J, Kim Y J and Yi G C 2008 *ACS Nano* **2** 637

[29] Jang J S, Joshi U A and Lee J S 2007 *J. Phys. Chem.* C **111** 13280

[30] Kenanakis G and Katsarakis N 2010 *Appl. Catal. A: Gen.* **378** 227

[31] Wu N Q, Wang J, Tafen D, Wang H, Zheng J G, Lewis J P, Liu X G, Leonard S S and Manivannan A 2010 *J. Am. Chem. Soc.* **132** 6679

[32] Liu Q, Zhou Y, Kou J H, Chen X Y, Tian Z P, Gao J, Yan S C and Zou Z G 2010 *J. Am. Chem. Soc.* **132** 14385

[33] Huang J, Ding K, Hou Y, Wang X and Fu X 2008 Synthesis and photocatalytic activity of Zn_2GeO_4 nanorods for the degradation of organic pollutants in water *ChemSusChem* **1** 1011

[34] Bi Y P and Ye J H 2009 *Chem. Commun.* **45** 6551

[35] Wang L, Wei H W, Fan Y J, Liu X Z and Zhan J H 2009 *Nanoscale Res. Lett.* **4** 558

[36] Shahid M, Shakir I, Yang S J and Kang D J 2010 *Mater. Chem. Phys.* **124** 619

[37] Berr M, Vaneski A, Susha A S, Rodríguez-Fernández J, Döblinger M, Jäckel F, Rogach A L and Feldmann J 2010 *Appl. Phys. Lett.* **97** 093108

[38] Vaneski A, Susha A S, Rodriguez-Fernandez J, Berr M, Jäckel F, Feldmann J and Rogach A L 2011 *Adv. Funct. Mater.* **21** 1547

[39] Berr M J, Wagner P, Fischbach S, Vaneski A, Schneider J, Susha A S, Rogach A L, Jäckel F and Feldmann J 2012 *Appl. Phys. Lett.* **100** 223903

[40] Berr M J, Vaneski A, Mauser C, Fischbach S, Susha A S, Rogach A L, Jäckel F and Feldmann J 2012 *Small* **8** 291

[41] Berr M *et al* 2012 *Nano Lett.* **12** 5903

[42] Schweinberger F F *et al* 2013 *J. Am. Chem. Soc.* **135** 13262

[43] Simon T *et al* 2014 *Nat. Mater.* **13** 1013

[44] Choi T, Lee S, Choi Y J, Kiryukhin V and Cheong S-W 2009 *Science* **324** 63

[45] Grinberg I *et al* 2013 *Nature* **503** 509

[46] Li H, Sang Y, Chang S, Huang X, Zhang Y, Yang R, Jiang H, Liu H and Wang Z L 2015 *Nano Lett.* **15** 2372

[47] Su R, Shen Y, Li L, Zhang D, Yang G, Gao C and Yang Y 2015 *Small* **11** 202

[48] Cui Y, Briscoe J and Dunn S 2013 *Chem. Mater.* **25** 4215

[49] Kirchartz T, Bisquert J, Mora-Seroc I and Garcia-Belmonte G 2015 *Phys. Chem. Chem. Phys.* **17** 4007

[50] Chen Y, Zhao H, Liu B and Yang H 2015 *Appl. Catal.* B **163** 189

[51] Bhavanasi V, Kusuma D Y and Lee P S 2014 *Adv. Energy Mater.* **4** 1400723

[52] Jeon C H, Lee Y S, Yee K J, Han J K and Bu S.D 2015 *Curr. Appl. Phys.* **15** 115

[53] Liew W H, Mirshekarloo M S, Chen S, Yao K and Tay F E H 2015 *Sci. Rep.* **5** 9790

[54] Liu M and Wang J 2015 *Sci. Rep.* **5** 7728

[55] Li H F, Zhang G H, Zheng Y, Wang B and Chen W J 2014 *Acta Mater.* **76** 472

[56] Wang J, Xu T, Shimada T, Wang X and Zhang T Y 2014 *Phys. Rev.* B. **89** 144102

[57] Yoo H, Bae C, Kim M, Hong S, No K, Kim Y and Shin H 2013 *Appl. Phys. Lett.* **103** 022902

[58] Zhao Y, Miao J, Meng X B, Weng F, Xu X G, Jiang Y and Wang S G 2013 *J. Mater. Sci. Mater. Electron.* **24** 1439

[59] Evarestov R A, Bandura A V and Kuruch D D 2013 *J. Comput. Chem.* **34** 175

[60] Han J K, Choi Y C, Kwak J H and Bu S D 2013 *Ferroelectrics* **454** 29

[61] Nuraje N and Su K 2013 *Nanoscale* **5** 8752

[62] Shimada T, Wang X, Kondo Y and Kitamura T 2012 *Phys. Rev. Lett.* **108** 067601

[63] Alexe M and Hesse D 2012 *Ferroelectrics* **433** 53

[64] Rorvik P M, Grande T and Einarsrud M A 2011 *Adv. Mater.* **23** 4007

[65] Wang C D, Lu Z Z, Yuan W X, Kwok S Y and Teng B H 2011 *Phys. Lett.* A **375** 3405

[66] Luo Y, Szafraniak I, Zakharov N D, Nagarajan V, Steinhart M, Wehrspohn R B, Wendorff J H, Ramesh R and Alexe M 2003 *Appl. Phys. Lett.* **83** 440

[67] Sastre F, Fornés V, Corma A and García H 2012 *Chem.—A Eur. J.* **18** 1820

[68] Sastre F, Corma A and García H 2012 *J. Am. Chem. Soc.* **134** 14137

[69] Sastre F, Corma A and García H 2012 *Appl. Catal. B: Environ.* **128** 84

[70] Dietl N, Schlangen M and Schwarz H 2012 *Angew. Chem. Int. Ed.* **51** 23

[71] Fresno F, Portela R, Suárez S and Coronado J M 2014 *J. Mater. Chem.* A **2** 2863

[72] Baltrusaitis J, Jansen I and Schuttlefield Christus J D 2014 *Catal. Sci. Technol.* **4** 2397

[73] Wada S I, Eto A and Wada K 1979 *J. Soil Sci.* **30** 347

[74] Barron P F, Wilson M A, Campbell A S and Frost R L 1982 *Nature* **299** 616

[75] Mukherjee S, Bartlow V M and Nair S 2005 *Chem. Mater.* **17** 4900

[76] Kang D Y, Zang J, Wright E R, McCanna A L, Jones C W and Nair S 2010 *ACS Nano* **4** 4897

[77] Theng B K G, Russell M, Churchman G J and Parfitt R L 1982 *Clays Clay Miner.* **30** 143

[78] Mukherjee S, Kim K and Nair S 2007 *J. Am. Chem. Soc.* **129** 6820

[79] Yucelen G I, Choudhury R P, Vyalikh A, Scheler U, Beckham H W and Nair S 2011 *J. Am. Chem. Soc.* **133** 5397

[80] Yucelen G I, Kang D Y, Guerrero-Ferreira R C, Wright E R, Beckham H W and Nair S 2012 *Nano Lett.* **12** 827

[81] Cradwick P D, Wada K, Russell J D, Yoshinaga N, Masson C R and Farmer V C 1972 *Nat. Phys. Sci.* **240** 187

[82] Bursill L A, Peng J L and Bourgeois L N 2000 *Phil. Mag. A* **80** 105

[83] Levard C, Rose J, Masion A, Doelsch E, Borschneck D, Olivi L, Dominici C, Grauby O, Woicik J C and Bottero J-Y 2008 *J. Am. Chem. Soc.* **130** 5862

[84] Konduri S, Mukherjee S and Nair S 2006 *Phys. Rev. B* **74** 033401

[85] Levard C *et al* 2010 *Chem. Mater.* **22** 2466

[86] Maillet P, Levard C, Larquet E, Mariet C, Spalla O, Menguy N, Masion A, Doelsch E, Rose J and Thill A 2010 *J. Am. Chem. Soc.* **132** 1208

[87] Maillet P, Levard C, Spalla O, Masion A, Rose J and Thill A 2011 *Phys. Chem. Chem. Phys.* **13** 2682

[88] Thill A, Maillet P, Guiose B, Spalla O, Belloni L, Chaurand P, Auffan M, Olivi L, and Rose J 2012 *J. Am. Chem. Soc.* **134** 3780

[89] Amara M-S, Paineau E, Bacia-Verloop M, Krapf M-E M, Davidson P, Belloni L, Levard C, Rose J, Launois P and Thill A 2013 *Chem. Commun.* **49** 11284

[90] Kang D Y, Zang J, Jones C W and Nair S 2011 *J. Phys. Chem. C* **115** 7676

[91] Zanzottera C, Armandi M, Esposito S, Gorrone E and Bonelli B 2012 *J. Phys. Chem. C* **116** 20417

[92] Zanzottera C, Vicente A, Celasco E, Fernandez C, Garrone E and Bonelli B 2012 *J. Phys. Chem. C* **116** 7499

[93] Bonelli B, Armandi M and Garrone E 2013 *Phys. Chem. Chem. Phys.* **15** 13381

[94] Bottero I, Bonelli B, Ashbrook S E, Wright, P A, Zhou W, Tagliabue M, Armandi M and Garrone E 2011 *Phys. Chem. Chem. Phys.* **13** 744

[95] Kang D Y, Brunelli N A, Yucelen G I, Venkatasubramanian A, Zang J, Leisen J, Hesketh P J, Jones C W and Nair S 2014 *Nat. Commun.* **5** 3342

[96] Amara M S, Paineau E, Rouzière S, Guiose B, Krapf M-E M, Taché O, Launois P and Thill A 2015 *Chem. Mater.* **27** 1488

[97] Katsumata K, Hou X, Sakai M, Nakajima A, Fujishima A, Matsushita N, MacKenzie K J D and Okada K 2013 *Appl. Catal. B: Environ.* **138** 243

[98] Marzan L L and Philipse A P 1994 *Colloid Surf. A* **90** 95

[99] Ma W, Yah W O, Otsuka H and Takahara A 2012 *J. Mater. Chem.* **22** 11887

[100] Ookawa M 2012 *Clay Minerals in Nature—Their Characterization, Modification and Application* ed M Valaskova (Rijeka, Croatia: InTech) p 2708

[101] Arancibia-Miranda N, Escudey M, Pizarro C, Denardin J C, García-González M T, Fabris J D and Charlet L 2014 *Mater. Res. Bull.* **51** 145

[102] Avellan A, Levard C, Kumar N, Rose J, Olivi L, Thill A, Chaurand P, Borschneck D and Masion A 2014 *RSC Adv.* **4** 49827

[103] Alvarez-Ramírez F 2007 *Phys. Rev. B* **76** 125421

[104] Guimarães L, Enyashin A N, Frenzel J, Heine T, Duarte H A and Seifert G 2007 *ACS Nano* **1** 362

[105] Li L, Xia Y, Zhao M, Song C, Li J and Liu X 2008 *Nanotechnology* **19** 175702

[106] Teobaldi G, Beglitis N S, Fisher A J, Zerbetto F and Hofer W A 2009 *J. Phys.: Condens. Matter* **21** 195301

[107] Zhao M, Xia Y and Mei L 2009 *J. Phys. Chem. C* **113** 14834

[108] Demichelis R, Noël Y, D'Arco P, Maschio L, Orlando R and Dovesi R 2010 *J. Mater. Chem.* **20** 10417

[109] Lourenço M P, Guimarães L, da Silva M C, de Oliveira C, Heine T and Duarte H A 2014 *J. Phys. Chem. C* **118** 5945

[110] Guimarães L, Pinto Y N, Lourenço M P and Duarte H A 2013 *Phys. Chem. Chem. Phys.* **15** 4303

[111] Alvarez-Ramírez F 2009 *J. Chem. Theory Comput.* **5** 3224

[112] Gustafsson J P 2001 *Clays Clay Miner.* **49** 73

[113] Yucelen G I, Choudhury R P, Leisen J, Nair S and Beckham H W 2012 *J. Phys. Chem. C* **116** 17149

[114] Poli E, Elliott J D, Hine N D M, Mostofi A A and Teobaldi G 2015 *Mater. Res. Innov.* **19** S272

[115] Bard A J 1979 *J. Photochem.* **10** 59

[116] Maeda K 2013 *ACS Catal.* **3** 1486

[117] Pacchioni G, Frigoli F, Ricci D and Weil J A 2000 *Phys. Rev. B* **63** 054102

[118] Stoneham A M, Gavartin J, Shluger A L, Kimmel1 A V, Muñoz Ramo D, Rønnow H M, Aeppli G and Renner C 2007 *J. Phys.: Condens. Matter* **19** 255208

[119] Lany S and Zunger A 2009 *Phys. Rev. B* **80** 085202

[120] Bowler D R and Miyazaki T 2012 *Rep. Prog. Phys.* **75** 036503

[121] Skylaris C K, Haynes P D, Mostofi A A and Payne M C 2015 *J. Chem. Phys.* **122** 084119

[122] Haynes P D, Skylaris C K, Mostofi A A and Payne M C 2006 *Phys. Status Solidi B* **243** 2489

[123] Hine N D M, Haynes P D, Mostofi A A, Skylaris K and Payne M C 2009 *Comput. Phys. Commun.* **180** 1053

[124] Hine N D M, Robinson M, Haynes P D, Skylaris C K, Payne M C and Mostofi A A 2011 *Phys. Rev. B* **83** 195102

[125] Kohn W 1996 *Phys. Rev. Lett.* **76** 3168

[126] Prodan E and Kohn W 2005 *Proc. Natl Acad. Sci. USA* **102** 11635

[127] Kohn W 1959 *Phys. Rev.* **115** 809

[128] des Cloizeaux J 1964 *Phys. Rev.* **135** A698

[129] Nencieu G 1983 *Commun. Math. Phys.* **91** 81

[130] He L and Vanderbilt D 2001 *Phys. Rev. Lett.* **86** 5341

[131] des Cloizeaux J 1964 *Phys. Rev.* **135** A685

[132] Ismail-Beigi S and Arias T A 1999 *Phys. Rev. Lett.* **82** 2127

[133] Payne M C, Teter M, Allan D C, Arias T A and Joannopoulos J D 1992 *Rev. Mod. Phys.* **64** 1045

[134] McWeeny R 1960 *Rev. Mod. Phys.* **32** 335

[135] Hernandez E and Gillan M J 1995 *Phys. Rev. B* **51** 10157

[136] Skylaris C K, Mostofi A A, Haynes P D, Dieguez O and Payne M C 2002 *Phys. Rev. B* **66** 035119

[137] Haynes P D, Skylaris C K, Mostofi A A and Payne M C 2006 *Chem. Phys. Lett.* **422** 345–9

[138] Ruiz-Serrano A, Hine N D M and Skylaris C K 2012 *J. Chem. Phys.* **136** 234101

[139] Skylaris K, Haynes D, Mostofi A A and Payne M C 2005 *J. Phys.: Condens. Matter* **17** 5757

[140] Ratcliff L E, Hine N D M and Haynes D 2011 *Phys. Rev. B* **84** 165131

[141] Zuehlsdorff T J, Hine N D M, Spencer J S, Harrison N M, Riley D J and Haynes P D 2013 *J. Chem. Phys.* **139** 064104

[142] Onida G, Reining L and Rubio A 2002 *Rev. Mod. Phys.* **74** 601

[143] Pickard C J 1997 *PhD Thesis* University of Cambridge

[144] Read A J and Needs R J 1991 *Phys. Rev. B* **44** 13071

[145] Motta C, Giantomassi M, Cazzaniga M, Gal-Nagy K and Gonze X 2010 *Comput. Mater. Sci.* **50** 698

[146] Perdew J, Burke K and Ernzerhof M 1996 *Phys. Rev. Lett.* **77** 3865

[147] Grimme S 2006 *J. Comput. Chem.* **27** 1787

[148] Klimeš J, Bowler D R and Michaelides A 2010 *J. Phys.: Condens. Matter* **22** 022201

[149] Gonze X, Stumpf R and Scheffler M 1991 *Phys. Rev.* B **44** 8503

[150] http://opium.sourceforge.net/sci.html

[151] Pfrommer B G, Côté M, Louie S G and Cohen M L 1997 *J. Comput. Phys.* **131** 233

[152] Hine N D M, Dziedzic J, Haynes P D, Skylaris C-K 2011 *J. Chem. Phys.* **135** 204103

[153] Wilkinson K A, Hine N D M and Skylaris C-K 2014 *J. Chem. Theory Comput.* **10** 4782

[154] Amara M S, Rouzière S, Paineau E, Bacia-Verloop M, Thill A and Launois P 2014 *J. Phys. Chem.* C **118** 9299

[155] Elliott J D, Hine N D M, Mostofi A A, Skylaris C-K and Teobaldi G 2015 to be submitted

[156] Scanlon D O *et al* 2013 *Nat. Mater.* **12** 798

[157] Perdew J P, Parr R G, Levy M and Balduz J L 1982 *Phys. Rev. Lett.* **49** 1691

[158] Sham L J and Schlüter M 1983 *Phys. Rev. Lett.* **51** 1888

[159] Heyd J, Peralta J E, Scuseria G E and Martin R L 2005 *J. Chem. Phys.* **123** 174101

[160] Paier J, Marsman M, Hummer K, Kresse G, Gerber I C and Ańgyań J G 2006 *J. Chem. Phys.* **124** 154709

[161] Paier J, Marsman M, Hummer K, Kresse G, Gerber I C and Ańgyań J G 2006 *J. Chem. Phys.* **125** 249901

[162] Tran F and Blaha P 2009 *Phys. Rev. Lett.* **102** 226401

[163] Mulliken R S 1955 *J. Chem. Phys.* **23** 1833

[164] Hine N D M, Avraam P W, Tangney P and Haynes P D 2012 *J. Phys. Conf. Ser.* **367** 012002

[165] Li G H and Gray K A 2007 *Chem. Phys.* **339** 173

[166] Bell R A, Payne M C and Mostofi A A 2014 *J. Chem. Phys.* **141** 164703

[167] Rienstra-Kiracofe J C, Tschumper G S and Schaefer H F III 2002 *Chem. Rev.* **102** 231–82

[168] Nitzan A 2006 *Chemical Dynamics in Condensed Phases: Relaxation, Transfer and Reactions in Condensed Molecular Systems* (Oxford: Oxford University Press)

[169] Lever G, Cole D J, Hine N D M, Haynes P D and Payne M C 2013 *J. Phys.: Condens. Matter* **25** 152101

[170] Cheng J and Sprik M 2012 *Phys. Chem. Chem. Phys.* **14** 11245

[171] Cheng J and Sprik M 2014 **26** 11245

[172] Nielsen M, Björketun M E, Hansen M H and Rossmeisl J 2015 *Surf. Sci.* **631** 2

[173] Gavartin J L and Shluger A L *Phys. Rev.* B **64** 245111

[174] Troisi A and Orlandi G 2006 *Phys. Rev. Lett.* **96** 086601

[175] Sleigh J P, McMahon D P and Troisi A 2009 *App. Phys.* A **95** 147

[176] Liu T and Troisi A 2014 *Adv. Funct. Mater.* **24** 925

[177] Janak J F 1978 *Phys. Rev.* B **18** 7165

[178] Perdew J P, Parr R G, Levy M and Balduz J L 1982 *Phys. Rev. Lett.* **49** 1691

[179] Perdew J P and Levy M 1983 *Phys. Rev. Lett.* **51** 1884

[180] Sau J D, Neaton J B, Choi H J, Louie S G and Cohen M L 2008 *Phys. Rev. Lett.* **101** 026804